ATLAS NOTE

ATL-PHYS-PUB-2009-003

April 26, 2009

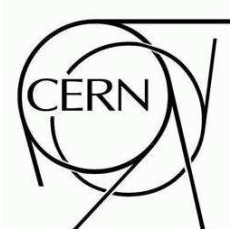

Calibration and Performance of the Electromagnetic Calorimeter

The ATLAS Collaboration[1)]

This note is part of CERN-OPEN-2008-020. This version of the note should not be cited: all citations should be to CERN-OPEN-2008-020.

[1)]This note prepared by M. Aharrouche, A. Ahmad, C. Anastopoulos, X. Anduaga, O. Arnaez, J.T. Baines, D. Banfi, K. Benslama, R.E. Blair, E.V. Bouhova-Thacker, C. Bourdarios, L. Carminati, J. Cochran, T. Cornelissen, R. Coura Torres, D. Damazio, A. De Santo, J. Del Peso, F. Derue, L. Di Ciaccio, K. Dindar, E. Dobson, M. Donega, M.T. Dova, M. Elsing, D. Emeliyanov, D. Enoque Ferreira de Lima, Y. Fang, O.L. Fedin, M. Fiascaris, H. Flacher, L.R. Flores Castillo, M.J. Flowerdew, T.M. Fonseca Martin, D. Froidevaux, O. Gaumer, I.L. Gavrilenko, R. Gonçalo, G. Gorfine, C. Goy, I. Grabowska-Bold, K. Grimm, H.K. Hadavand, J. Haller, M. Hance, J. Hoffman, T. Hryn'ova, D. Joffe, A. Kaczmarska, V. Kartvelishvili, A. Kasmi, R. Kehoe, N. Kerschen, G. Khoriauli, G. Kilvington, H. Kim, J. Kirk, G.P. Kirsch, K. Koeneke, T. Koffas, I. Koletsou, N. Konstantinidis, V.V. Kostyukhin, S. Laplace, F. Ledroit-Guillon, J.S.H. Lee, D. Lelas, T. Lenz, Z. Liang, W. Liebig, M. Losada, I. Ludwig, E. Lytken, H. Ma, N. Makovec, V.P. Maleev, L. Mandelli, J.-F. Marchand, F.F. Martin, S. Mättig, B.R. Mellado Garcia, F. Monticelli, D. Moreno, A.K. Morley, E.J.W. Moyse, G.A. Navarro, E. Nebot, C. Nelson, V.E. Ozcan, E. Paganis, F. Parodi, J. Parsons, V. Perez Reale, T.C. Petersen, G. Pinzon, A. Poppleton, K. Prokofiev, S. Rajagopalan, I. Riu Dachs, D. Rodriguez, Y. Rodriguez, S. Rosati, D. Rousseau, A. Salzburger, H. Sandaker, C. Santamarina Rios, C. Schiavi, C. Schmitt, S. Sivoklokov, S. Snyder, M.R. Sutton, M.C. Tamsett, J. Tojo, M.F. Tripiana, V. Tsulaia, E. Turlay, G. Unal, M. Wang, A.T. Watson, A.R. Weidberg, M. Wielers, A. Wildauer, E. Woehrling, X. Wu, J. Yu, D. Zerwas, N. Zhou, and H.Z. Zhu.

Abstract

This note describes the calibration of electromagnetic clusters, as implemented in current releases of the ATLAS reconstruction program. A series of corrections are applied to calibrate both the energy and position measurements; these corrections are derived from Monte-Carlo simulations and validated using test-beam data. The possibility of obtaining inter-calibration energy corrections from $Z \rightarrow ee$ data is also discussed.

1 Introduction

In order to realise the full physics potential of the LHC, the ATLAS electromagnetic calorimeter must be able to identify efficiently electrons and photons within a large energy range (5 GeV to 5 TeV), and to measure their energies with a linearity better than 0.5%. The W boson mass measurement, not considered here, will require better precision.

The procedure to measure the energy of an incident electron or photon in the ATLAS electromagnetic (EM) calorimeter has been described in Ref. [1]. Each step of the energy reconstruction has been validated by a series of beam tests over many years, both using only the calorimeter [2, 3] and also combined with representative components from all detector sub-systems. This has allowed considerable refinement of the calorimeter simulation. This simulation is then used to model the behaviour of the full detector.

One of the key ingredients for the description of the detector performance is the amount and position of the upstream material. The understanding of the ATLAS detector geometry has also made progress over the years; an overview of the present knowledge of the detector and its expected performance can be found in [4]. The amount of material in front of the calorimeter for the as-built detector is significantly larger than was initially estimated; this leads to larger energy losses for electrons and to a larger fraction of photons converting (see Figs. 1 and 2).

The standard ATLAS coordinate system is used: the beam direction defines the z-axis, and the x-y plane is transverse to the beam direction. The azimuthal angle ϕ is measured around the beam axis and the polar angle θ is the angle from the beam axis. The pseudorapidity is defined as $\eta \equiv -\ln(\tan(\theta/2))$.

1.1 Electron and photon candidates

The "sliding window" algorithm [5] is used to find and reconstruct electromagnetic clusters. This forms rectangular clusters with a fixed size, positioned so as to maximise the amount of energy within the cluster. An alternate algorithm is available which forms clusters based on connecting neighbouring cells until the cell energy falls below a threshold; this is not used by the default electron and photon reconstruction. The optimal cluster size depends on the particle type being reconstructed and the calorimeter region: electrons need larger clusters than photons due to their larger interaction probability in the upstream material and also due to the fact that they bend in the magnetic field, radiating soft photons along a range in ϕ. Several collections of clusters are therefore built by the reconstruction software, corresponding to different window sizes. These clusters are the starting point of the calibration and selection of electron and photon candidates.

One of the recent improvements in the calibration procedure is that electron and photon candidates are treated separately. For each of the reconstructed clusters, the reconstruction tries to find a matching track within a $\Delta\eta \times \Delta\phi$ window of 0.05×0.10 with momentum p compatible with the cluster energy E ($E/p < 10$ [6, 7]). If one is found, the reconstruction checks for presence of an associated conversion. An electron candidate is created if a matched track is found and no conversion is flagged. Otherwise, the candidate is classified as a photon.

This early classification allows applying different corrections to electron and photon candidates. It is the starting point of a more refined identification based largely on shower shapes, described in companion notes [6, 7]. Four levels of electron quality are defined (loose, medium, tight, and tight without isolation). The available photon selection corresponds to the tight electron selection (excluding tracking requirements). The medium and tight selections are used in some parts of the calibration analysis described in this note. But the corrections derived are then applied to all electron and photon candidates.

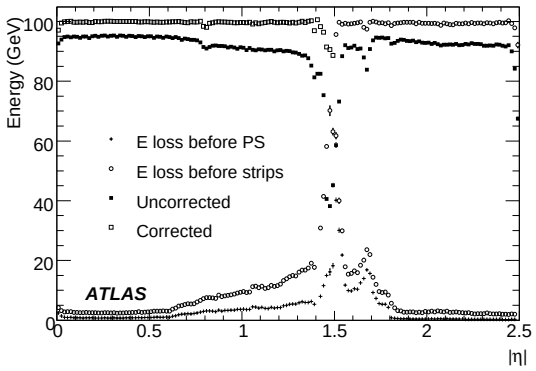

Figure 1: Average energy loss vs. $|\eta|$ for $E = 100$ GeV electrons before the presampler/strips (crosses/open circles), and reconstructed energies before/after (solid/open boxes) corrections.

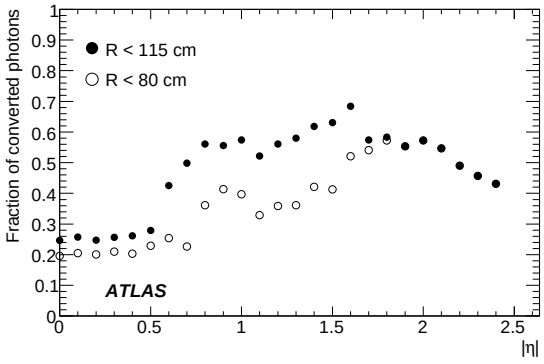

Figure 2: Fraction of photons converting at a radius of below 80 cm (115 cm) in open (full) circles, as a function of $|\eta|$ [4].

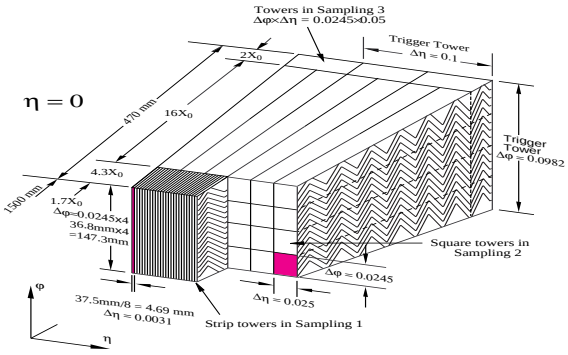

Figure 3: Sketch of the accordion structure of the EM calorimeter [8].

	$\|\eta\|$ range	Cell η size	
		Layer 1	Layer 2
Barrel	0–1.4	0.025/8	0.025
	1.4–1.475	0.025	0.075
end-cap	1.375–1.425	0.05	0.05
	1.425–1.5	0.025	0.025
	1.5–1.8	0.025/8	0.025
	1.8–2.0	0.025/6	0.025
	2.0–2.4	0.025/4	0.025
	2.4–2.5	0.025	0.025

Table 1: Calorimeter η granularity in layers 1 and 2.

1.2 Calorimeter granularity

The electromagnetic calorimeter (Fig. 3) was designed to be projective in η, and covers the pseudorapidity range $|\eta| < 3.2$. Precision measurements are however restricted to $|\eta| < 2.5$; regions forward of this are outside of the scope of this note. The calorimeter is installed in three cryostats: one containing the barrel part ($|\eta| < 1.475$), and two which each contain the two parts of the end-cap ($1.375 < |\eta| < 3.2$). Its accordion structure provides complete ϕ symmetry without azimuthal cracks. The total thickness of the calorimeter is greater than 22 radiation lengths (X_0) in the barrel and greater than $24X_0$ in the end-caps. It is segmented in depth into three longitudinal sections called layers, numbered from 1 to 3 outwards from the beam axis. These layers are often called “front” (or “strips”), “middle,” and “back.” The η granularity of the calorimeter for the front and middle layers is shown in Table 1. The ϕ size of cells is 0.025 in layer 2 and 0.1 in layer 1. Layer 3 has a granularity of $\Delta\eta \times \Delta\phi = 0.050 \times 0.025$. For $|\eta| < 1.8$, a presampler detector is used to correct for the energy lost by electrons and photons upstream of the calorimeter. All these regions must be treated separately in deriving the individual corrections.

The effect of the choice of cluster size on electron and photon energy reconstruction has been studied in Refs. [1] and [8]. These results are still the baseline of the present software. For electrons, the energy in the barrel electromagnetic calorimeter is collected over an area corresponding to 3×7 cells in the middle layer, i.e. $\Delta\eta \times \Delta\phi = 0.075 \times 0.175$. For unconverted photons, the area is limited to 3×5 cells in

the middle layer, whereas converted photons are treated like electrons. The cluster width in η increases with increasing $|\eta|$; therefore, an area of 5×5 cells in the middle layer is used for both electrons and photons in the end-cap calorimeter.

1.3 Geometries and data sets

The present knowledge of the detector geometry, resulting from the detector survey, is described in [4] (Sec. 9). But even before the final survey, it was known that the inner detector services located in the crack region would be wider than originally expected, and that the end-cap electromagnetic calorimeter would be shifted by about 4 cm, compared to the nominal (and pointing) geometry described in Ref. [1]. This is taken into account in the simulation, and is treated as a misalignment in the cell calibration procedure described below.

High statistics samples of single electrons and photons, processed with the full detector simulation based on GEANT 4.7 [9], were used to derive and study the corrections. Two detector geometries are available. The first is the "ideal geometry," which contains the best knowledge of the dead material, but which has no misalignments except for the 4 cm shift of the end-caps. The data sets based on this geometry are used to derive the corrections and for most of the performance studies. The second available geometry is a distorted one, in which extra material is added between the tracking detectors and the calorimeters, and in which misalignments are introduced. For example, the amount of material in the inner detector has increased in some regions by up to 7% of a radiation length for positive ϕ, and the density of material in the gap between the barrel and end-cap cryostats has increased by a factor of 1.7. The distorted data-sets using this geometry are used to estimate systematic uncertainties and to check the sensitivity of the methods to additional material. In addition to these single-particle data sets, $Z \rightarrow ee$ decays are also available.

The standard calorimeter reconstruction for simulated data includes the effects of possible cell-level miscalibrations by smearing the measured energy of each cell (by about 0.7%), therefore increasing the constant term of the energy resolution. (The fractional energy resolution is conventionally parametrised as $\sigma(E)/E = a/E \oplus b/\sqrt{E} \oplus c$, where a is the noise term, b is the sampling term and c is the constant term.) Unless otherwise stated, the results in this note do not include this additional smearing, and therefore correspond to assuming a perfect cell-level calibration.

1.4 Energy and position reconstruction

The calibration of the LAr calorimeter is factorised into a channel-by-channel calibration of the electronics readout and an overall energy scale determination.

The first step, often called "electronics calibration", converts the raw signal extracted from each cell (in ADC counts) into a deposited energy. The method used for this step, which is beyond the scope of this note, was described in Ref. [1]. It was refined and validated when final barrel and end-cap modules were studied in test beams [2, 3]. In the past two years, the experience gained and the algorithm developed were integrated into the standard ATLAS calibration software [10].

The second step deals with clusters. The energies deposited in the cells of each individual layer of a cluster are summed, and an energy-weighted cluster position is calculated for each layer. There are several important effects which must then be understood:

- Due to the accordion geometry, the amount of absorber material crossed by incident particles varies as a function of ϕ. This produces a ϕ modulation of the reconstructed energy.

- The shower is not fully contained in the η window chosen for clusters, and the cells have a finite granularity. This introduces a modulation in the energy and a bias in the measured position ("S-shape") which depend on the particle impact point within a cell.

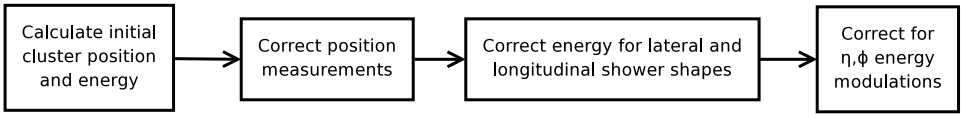

Figure 4: Cluster correction steps.

- A perfectly projective particle, coming from the origin of the coordinate system, intersects the calorimeter at the same η position in all layers. The luminous region, however, extends significantly in z; a particle from a vertex away from the origin intersects the calorimeter at slightly different η positions in each layer. Properly combining these η measurements requires an accurate parametrisation of the shower depth within each layer.

An early study of these corrections, using both simulation and test beam data, can be found in [11]. The present prediction of these effects and their dependencies on the impact point and energy of the incident particle are described in detail in this note.

The measured energy and position of EM clusters are corrected as described below (see Fig. 4). The required scale of the correction is illustrated by the upper points in Fig. 1, which shows the reconstructed energies of $E = 100$ GeV electrons before and after calibration. It is about 10% over most of the calorimeter, but is larger in the transition region between cryostats.

- To start with, the energies in the cluster cells are summed, and an energy weighted (η, ϕ) position is calculated for each calorimeter layer. Before applying the cluster corrections, the energy resolution has a constant term of about 0.65% (quoted for photons at $|\eta| = 0.3$).

- As the first step, corrections are applied to the cluster position, measured in each layer. These are described in Sec. 2. The position measurements from the first two layers are then combined to define the shower impact point in the calorimeter, which can then be used for energy reconstruction.

- The next step is to combine the energies deposited in each layer. Two separate procedures have been developed to do this which are described in Secs. 3.1 and 5. In the first one, per-layer energy coefficients, called longitudinal weights, are adjusted to optimise at the same time the energy resolution and the linearity of the response. In the second one, the simulation is used to correct for different types of energy loss one by one, by correlating each of them with measured observables. The corrections are calculated separately for electrons and photons, and determined as a function of $|\eta|$. This reduces the local constant term to about 0.61%.

- The third step, described in Sec. 3.2, uses the shower impact point to correct the total energy for modulations in η and ϕ. This reduces the local constant term to about 0.43%.

In spite of the skill and care put into the detector construction, calibration, and operation, some local or "medium range" inhomogeneities in the calorimeter response have to be expected: localised high-voltage or temperature effects or unexpected additional dead material must be detected and corrected for using data. It is planned to use $Z \rightarrow ee$ decays to measure and correct for such effects and to help fix the absolute energy scale. The method developed and the precision expected are described in Sec. 6.

2 Cluster position measurement

The position of a cluster is measured in η and ϕ. The positions are first calculated independently for each calorimeter layer as the energy-weighted barycenters of all cluster cells in the layer. (The barrel and endcap are also treated separately at this stage.) Secondly, the individual layer measurements are corrected

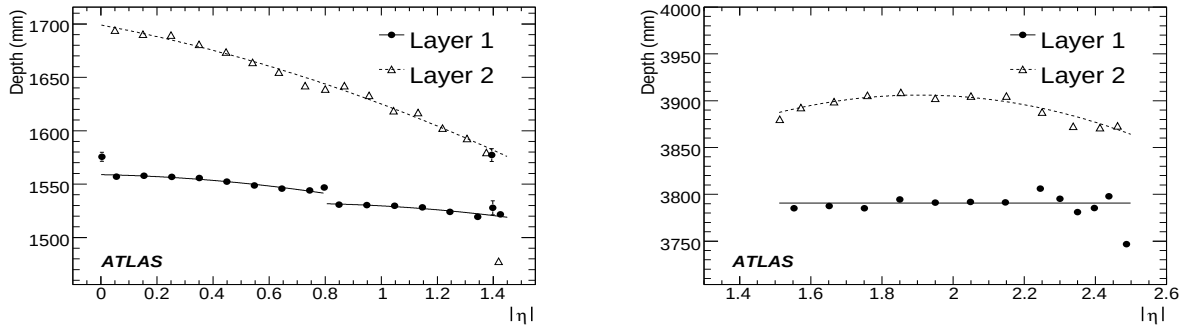

(a) Barrel.

(b) End-cap.

Figure 5: Calorimeter depths versus $|\eta|$ for layers 1 and 2 and for 100 GeV photons. The points show the derived optimal depths, and the curves are piecewise polynomial fits to the points. For layer 2 of the barrel, a single curve yielded an adequate fit across $|\eta| = 0.8$; this may be revisited in future versions. From 100 GeV photons.

for known systematic biases. Finally, the position measurements from layers 1 and 2 are combined to produce the overall cluster position. The position corrections are derived using single-particle electron and photon data samples. Each sample is mono-energetic, and the available samples span the range 5–1000 GeV.

The η positions that are calculated at this stage are "detector"-η, corresponding to the angle that would be made by a particle originating from the origin of the detector coordinate system. In order to properly compare the calculated detector-η positions with the η of a generated incident particle, which will in general have its production vertex offset in z from the detector origin, one must assume a depth for each calorimeter layer. Here, "depth" refers to the radial distance from the beam axis for the barrel calorimeter, and to the distance from the $x-y$ plane passing through the origin for the end-cap calorimeter. The depths used are those which optimise the η-position resolution; they are shown in Fig. 5.

2.1 η position correction (S-shape)

The cluster η position is first calculated in each layer as the energy-weighted barycenter of the cluster cells in that layer. (In layer 1, only the three strips around the cluster center are used, regardless of the specified cluster size.) Due to the finite granularity of the readout cells, these measurements are biased towards the centers of the cells. For examples, see Fig. 6. This figure plots the difference in η between the incident particle and the reconstructed cluster ($\Delta\eta = \eta_{\text{true}} - \eta_{\text{reco}}$) as a function of v, the relative η offset of the cluster within the cell, which varies from $-1/2 \ldots 1/2$ across the cell. (The sign of $\Delta\eta$ is inverted for negative η, and in plots it is usually shown as a fraction of the cell η width.) The general functional form shown in this figure is often referred to as "S-shape".

Figure 6 shows the correction averaged over an $|\eta|$ range. The actual correction, however, varies continuously over η, due to changes in the detector geometry (the corrections change to a much greater extent near discontinuities in the calorimeter). For example, the calorimeter cells are not perfectly projective (as the inner and outer cell faces are parallel to the beam-line, rather than being perpendicular to a line from the detector origin); this induces a bias away from the center of the calorimeter. The correction will also depend on the cluster energy, as that affects the average shower depth.

To derive the correction, the calorimeter is divided in η into regions based on where the behaviour of the correction changes discontinuously. Within each region, an empirical function is constructed to

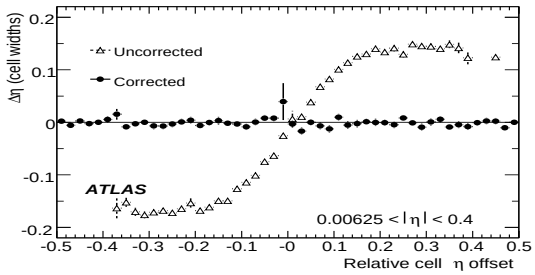

(a) Layer 1, barrel.

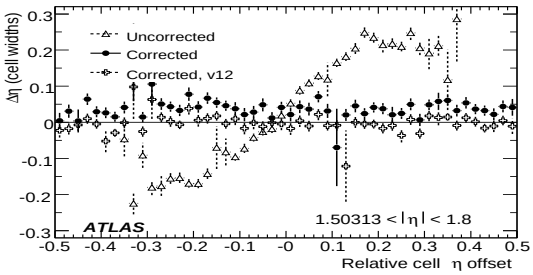

(b) Layer 1, end-cap.

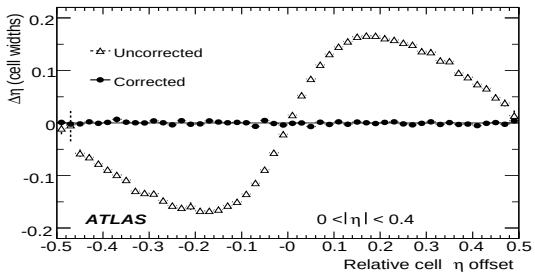

(c) Layer 2, barrel.

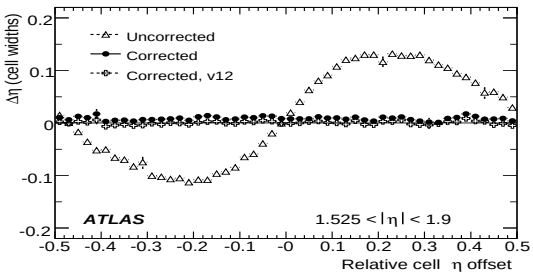

(d) Layer 2, end-cap.

Figure 6: $\Delta\eta$ versus v before and after correction for different regions and for 100 GeV electrons. Note the small systematic offset in the end-cap due to a change in the end-cap geometry since the corrections were derived. For comparison, the "v12" points show results reconstructed using the same geometry as that used to derive the corrections.

describe the correction, and an unbinned fit is performed to simulated data for a particular cluster size, type, and energy.

The function used for the empirical fit is of the form

$$f(v) = A\tan^{-1}Bv + Cv + D|v| + E, \tag{1}$$

where $-1/2 \leq v \leq 1/2$ across a cell (for the actual fit, the parameters are redefined to reduce correlations). To turn this into a function of η, the fit parameters are written as polynomials (usually of second or third degree) in $|\eta|$:

$$A = \sum_i a_i |\eta|^i, \tag{2}$$

and similarly for the other parameters. The fit parameters are then the coefficients a_i, b_i, etc.

One feature to note about this function is that, in general, $f(-1/2) \neq f(1/2)$, so that it will be discontinuous crossing a cell boundary. For layer 1, this is usually acceptable, since reconstructed cluster positions cluster well away from the cell boundary (Fig. 7(a)). However, in layer 2, the distribution of reconstructed cluster positions remains populated across the cluster boundary (Fig. 7(b)). Therefore, for layer 2, the function is modified so that $f(-1/2) = f(1/2)$.

In some cases, there is still a significant periodic residual after fitting to this form; in such cases, an additional general trigonometric term is added to the fit:

$$f'(v) = f(v) + \alpha\cos(\beta\pi v + \gamma). \tag{3}$$

Finally, a few regions near the calorimeter edges do not exhibit the S-shape form; a general polynomial is used as the empirical function there.

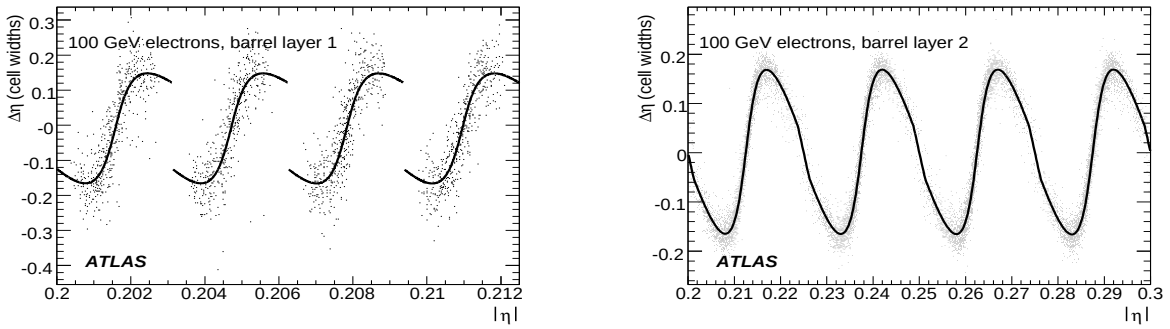

(a) Barrel layer 1

(b) Barrel layer 2

Figure 7: $\Delta\eta$ versus $|\eta|$ in layers 1 and 2 of the barrel, along with the empirical fit function.

The correction is evaluated separately for each cluster size and type (electrons, photons). The difference in the correction between electrons and photons is a few percent, and there is about a 10% difference between 5×5 and $3 \times N$ clusters.

The correction also depends on energy; over the range 25–1000 GeV, the required correction varies by $\sim 20\%$. To apply the correction for a given cluster, the correction is first tabulated for each of the energies for which simulated data samples were available. The final correction is then found by doing a cubic polynomial interpolation within this table. Note a subtlety here: the energies at which the corrections are tabulated are the true cluster energies. However, when the correction is applied, only the reconstructed cluster energy is known. Since the position corrections are done before the energy corrections, the reconstructed cluster energy will be systematically lower than the true energy. If this were used for the interpolation, this would bias the position measurements. So, for the purpose of this interpolation, a crude energy correction is performed by scaling the reconstructed cluster energy by the ratio of the true to reconstructed energy observed in a 100 GeV sample, parametrised as a function of $|\eta|$. This energy correction is used only for the energy interpolation of the position corrections.

Plots of $\Delta\eta$ before and after corrections for several regions are shown in Fig. 6. Note that since the present corrections were derived, the simulated detector geometry was changed slightly in the end-cap, in order to match more closely the as-built detector. This results in a small systematic offset of $O(10^{-4})$ in these regions.

The η position resolution for photons versus $|\eta|$ is shown for the two main calorimeter layers (strips and middle) in Fig. 8. The resolution is fairly uniform as function of $|\eta|$ and is 2.5–3.5 $\times 10^{-4}$ for the strips (which have a size of 0.003 in η in the barrel electromagnetic calorimeter) and 5–6 $\times 10^{-4}$ for the middle-layer cells (which have a size of 0.025 in η). The regions with worse resolution correspond to the barrel/end-cap transition region and, for the strips, to the region with $|\eta| > 2$, where the strip granularity of the end-cap calorimeter becomes progressively much coarser.

2.2 ϕ position correction

The measurement of the cluster ϕ position must also be corrected. These corrections are applied only in calorimeter layer 2 (the ϕ granularity is best in this layer). As opposed to the η direction, the accordion geometry results in more energy sharing between cells in the ϕ direction, which washes out the S-shape in this direction. There is, however, a small bias in the ϕ measurement which depends on the average shower depth with respect to the accordion structure (and thus on $|\eta|$). A profile plot of $\Delta\phi = \phi_{\text{true}} - \phi_{\text{reco}}$ before the correction is shown in Fig. 9. (The sign of the offset is flipped for $\eta < 0$, as the two halves of the calorimeter are identical under a rotation.) The discontinuity at $|\eta| = 0.8$, where the absorber

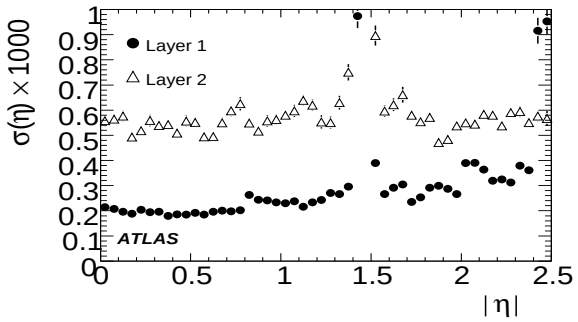

Figure 8: Expected η position resolution versus $|\eta|$ for $E = 100$ GeV photons for the two main layers of the barrel and end-cap EM calorimeters [4].

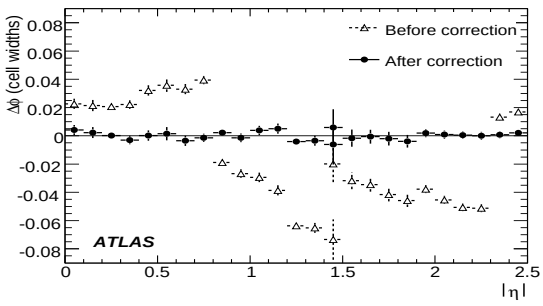

Figure 9: Profile plot of $\Delta\phi$ versus $|\eta|$ before (triangles) and after (circles) correction. For 100 GeV electrons.

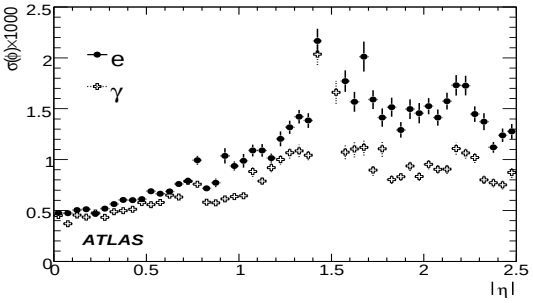

Figure 10: Expected ϕ position resolution as a function of $|\eta|$ for electrons and photons with an energy of 100 GeV.

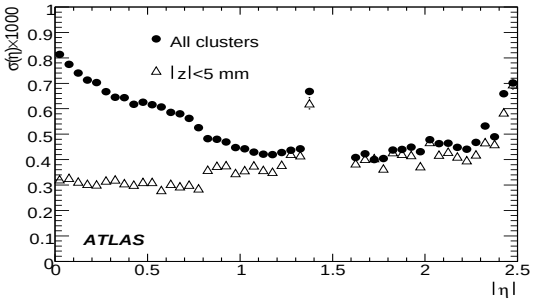

Figure 11: Resolution of η position measurement from layers 1 and 2 combined for 100 GeV photons.

thickness and the middle layer depth change, is clearly visible.

The correction derived here is symmetric in ϕ. In the real detector, the absorbers sag slightly due to gravity, causing a ϕ-dependent modulation in the ϕ offset with a maximum value of about 0.5 mrad [8]. This has not been included in the present simulations, and it is therefore not taken into account in this correction. Studies have shown, however, that the extra smearing of the position measurement from this effect has a negligible contribution to the widths of the invariant mass distributions of e^+e^- pairs. (These studies were performed by generating decays of massive particles using a toy Monte Carlo, smearing the decay products with energy and angular resolutions roughly appropriate to ATLAS, and comparing the widths of the resulting invariant mass distributions before and after shifting the ϕ positions by $A\cos\phi$. No significant broadening was observed for $A < 50$ mrad.) The contribution of this effect to the constant term of the energy resolution has not been studied quantitatively, but should also be small.

To produce a correction, the data are binned in η. The result for one sample is shown in Fig. 9. This function is interpolated in η; it is then also interpolated in energy as for the η position correction.

The ϕ position resolution versus $|\eta|$ is shown for calorimeter layer 2 in Fig. 10. Electron clusters, which get smeared in the ϕ direction as they radiate while propagating through the magnetic field, have a worse ϕ position resolution than do photon clusters. A discontinuous step is seen in the resolution at $|\eta| = 0.8$, where the absorber thickness changes, and the resolution is worst in the transition region between the cryostats.

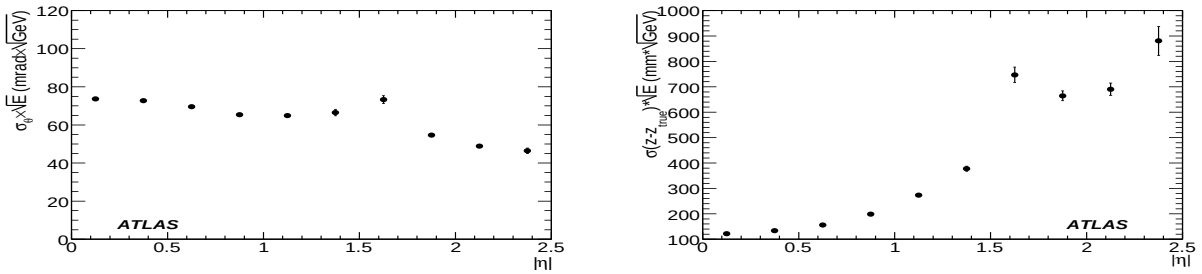

(a) Angular resolution.

(b) Vertex resolution.

Figure 12: Angular and vertex resolution as functions of $|\eta|$ (Gaussian fits), multiplied by $\sqrt{E}$.

2.3 Position measurement combination

The individual layer η and ϕ measurements are combined to produce the overall η and ϕ for a cluster. For ϕ, only layer 2 is used, so the combination is trivial except in the overlap region, where the energy-weighted average of the barrel and end-cap ϕ measurements is used. For η, both layer 1 and layer 2 are averaged. However, layer 1 is weighted three times as much as layer 2 to roughly take into account the better resolution in layer 1. This prescription, which does not use the actual position resolutions and does not account for correlations, is known to be suboptimal and will be improved in future software versions.

Note that the η combination implicitly assumes that the incoming particle is projective. If its production vertex is shifted from the origin, then the combined η will be biased. This is illustrated in Fig. 11, which shows the resolution of the combined cluster η measurement. Here, the measured cluster η is compared to the η position of the calorimeter intersected by the true particle track at a depth corresponding to the cluster barycenter. This is shown both for all clusters and for clusters with the z position of the production vertex within 5 mm of the detector center.

2.4 Shower direction

At high luminosity, the inner detector cannot accurately determine the interaction vertex due to the large number of additional interactions. This is an issue for the reconstruction of a $H \to \gamma\gamma$ signal. For this analysis, achieving the best possible resolution on the invariant mass of the photon pair is crucial for separating the signal peak from the continuum background. If the z-position of the interaction vertex is unknown, then there will be a large uncertainty in the polar angle of the photons and thus in the pair invariant mass. We can, however, recover information about the incidence angle of the photons by comparing the impact points that are reconstructed in the first and second layers of the EM calorimeter. To do this, we need to know the photon η position and the shower barycenter in each of the two layers (Fig. 5). We can then draw a straight line between these two (η, depth) points; extending this line to the beam axis gives an estimate of the position of the interaction vertex.

Here, this method is applied to single photons with energies compatible with photons from $H \to \gamma\gamma$ decays. For $m_H = 120$ GeV, these photons are predominantly in the range $50 - 100$ GeV. Figure 12 shows the resolutions of the photon angle and the interaction vertex measurements as functions of $|\eta|$. Figure 13 shows the same resolution as a function of the photon energy, for $|\eta| < 0.5$.

3 Cluster energy measurement

Most of the energy of an electromagnetically interacting particle is deposited in the sensitive volume of the calorimeter, including the lead absorbers and the liquid-argon gaps. A small fraction is deposited in

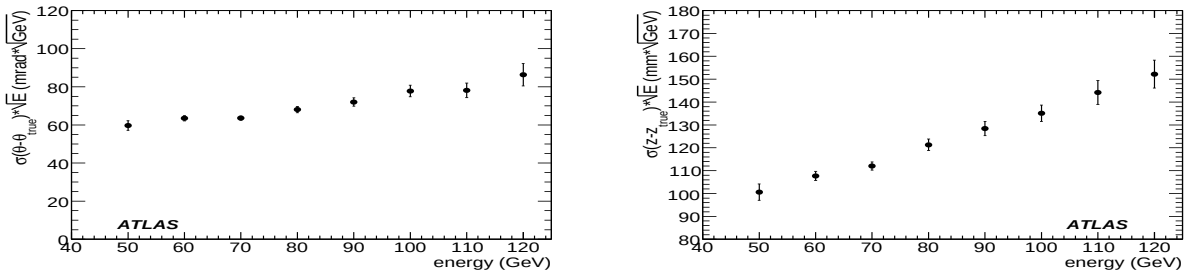

(a) Angular resolution.

(b) Vertex resolution.

Figure 13: Angular and vertex resolution as functions of E (Gaussian fits), for $|\eta| < 0.5$.

non-instrumented material in the inner detector, the cryostats, the solenoid, and the cables between the presampler and the first EM calorimeter layer. Energy also escapes from the back of the calorimeter.

The cluster energy is calculated as a linearly weighted sum of the energy in each of the three calorimeter layers plus the presampler. The factors applied to the four energies are called longitudinal weights and their purpose is to correct for the energy losses, providing optimum linearity and resolution.

The ATLAS longitudinal weighting method was first described in Ref. [8]. However, recent ATLAS test beam analyses [2, 3, 12] provided simple extensions of the technique. They also allowed validating this method with real data.

The first section below describes the weighting correction that is performed in current versions of the reconstruction, called the 4-weight method. This is followed by a description of the corrections for η- and ϕ-dependent modulations in the energy. A more advanced energy-dependent calibration scheme, called the calibration hit method, is described separately in Section 5.

3.1 4-weight method

The weighting method described in this section is is a modification of that described in Ref. [8] and is currently the default in ATLAS reconstruction. The weights used are functions only of $|\eta|$; no energy dependencies are used. The method could be readily extended to include ϕ- and energy-dependent weights in order to minimise residual non-linearities. The reconstructed energy is given by

$$E_{\text{reco}} = A(B + W_{\text{ps}}E_{\text{ps}} + E_1 + E_2 + W_3E_3), \tag{4}$$

where E_{ps} and $E_{1\ldots3}$ are the cluster energies in the presampler and the three layers of the calorimeter (including sampling fractions). The offset term B corrects for upstream energy losses for which the corresponding electron has not reached the presampler (PS). In the limiting case of no energy in the PS, this offset corresponds to the energy an electron loses before it undergoes a hard bremsstrahlung for which the resulting photon passes through the PS without converting (i.e., no energy recorded in the PS). The parameters A, B, W_{ps}, and W_3 are calculated by a χ^2 minimisation of $(E_{\text{true}} - E_{\text{reco}})^2/\sigma(E_{\text{true}})^2$ using Monte Carlo single particle samples, where $\sigma(E_{\text{true}})$ is a parametrisation of the expected energy resolution. This minimisation is done for separate $|\eta|$ bins, defined by the $\Delta\eta = 0.025$ granularity of the second layer of the calorimeter. Equal-sized samples with energies between 10 and 200 GeV are combined for the fits (the linearity of low energy points could be improved by using more events at those energies.) The fits are done separately for each cluster size and particle type (electron and photon).

A special parametrisation is applied in the gap region between the barrel and end-cap calorimeters ($1.447 < |\eta| < 1.55$), within which the parametrisation of Eq. (4) is not adequate. Moreover, this region is instrumented with scintillator tiles that can be used to recover some of the energy lost in the gap. The

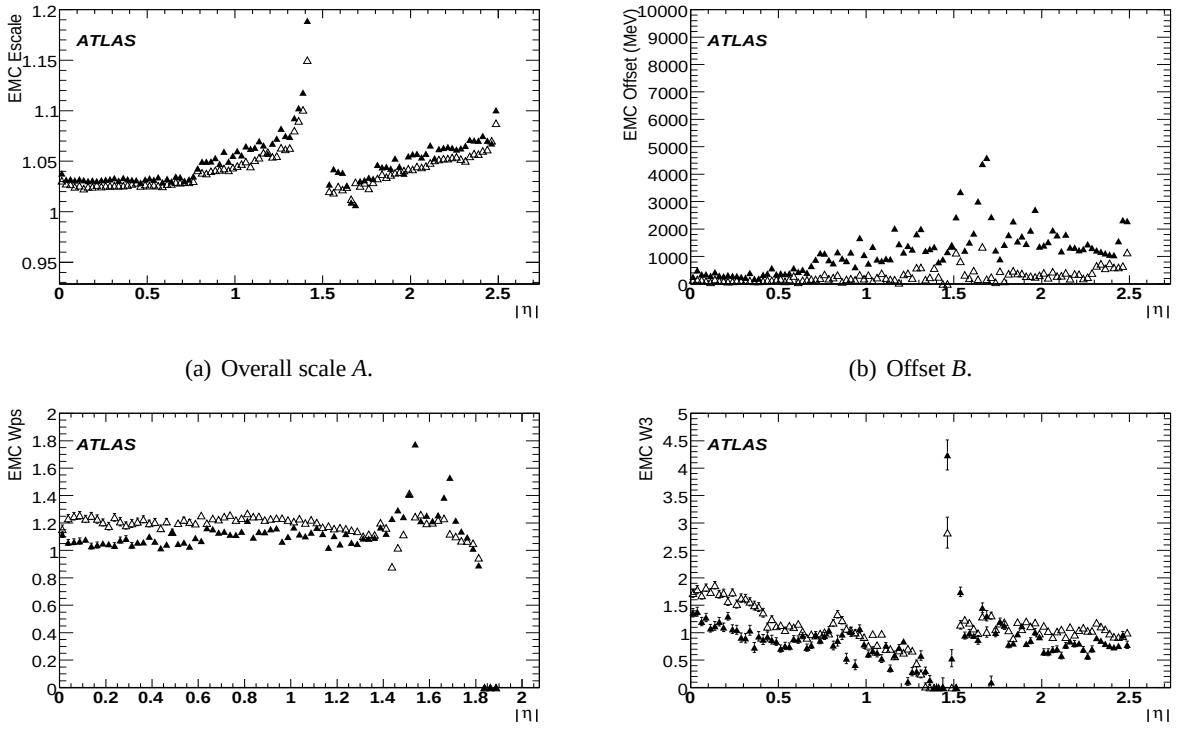

(a) Overall scale A.

(b) Offset B.

(c) Longitudinal weight $W_{\rm ps}$.

(d) Longitudinal weight W_3.

Figure 14: Fitted longitudinal weights for electrons (solid) and photons (open) as functions of $|\eta|$.

parametrisation used in the crack is

$$E_{\rm reco} = A(B + E_b + E_e + W_{\rm scint}E_{\rm scint}), \tag{5}$$

where E_b and E_e are the energies the cluster deposits in the barrel and end-cap calorimeters, respectively. $E_{\rm scint}$ is the scintillator energy, and $W_{\rm scint}$ the weight applied to it. This parametrisation is found to perform significantly better than that used in [1].

The longitudinal weights in Eq. (4) were extracted for electrons and photons and are shown as a function of $|\eta|$ in Fig. 14. In Fig. 14(a) one can see that the overall scale A for electrons (solid) is larger than that for photons. The reason is due to the fact that photons travel on average $9/7X_0$ before they start losing energy. This effect is close to 1% in the middle of the barrel and increases with the increase of upstream material. The offset term B is shown in Fig. 14(b); photons have a very small offset, as expected. (Future versions of the correction will use larger statistics to reduce the scatter observed in the fit results.) The PS weight $W_{\rm ps}$ shown in Fig. 14(c) is the usual factor applied to preshower/presampler energy responses to correct for upstream losses. Finally, in Fig. 14(d), W_3 is a weight applied to the last calorimeter layer to correct for energy leakage behind the calorimeter.

Detailed studies have revealed that the physical meaning attributed to these weights is only approximate. For example, the weights compensate for losses after the PS via the minimisation procedure. In addition, the weights have a non-negligible energy dependence. However, this energy dependence does not result in large non-linearities because the weights adjust their values to compensate. These effects are more evident at low energies $E < 15$ GeV, and with large amounts of upstream material. A more rigorous treatment of the longitudinal weighting is presented in Sec. 5.

The performance of this method is shown in Sec. 4

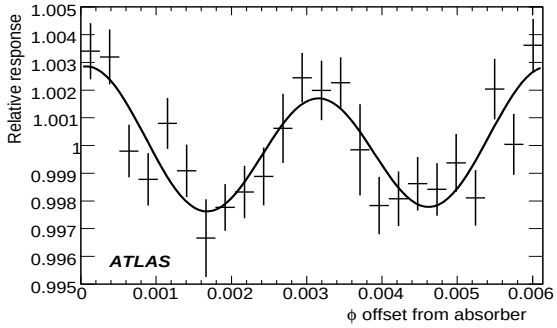

Figure 15: Energy modulation in ϕ for 200 GeV 3×7 electrons with $0.2 < |\eta| < 0.4$, along with the modulation fit.

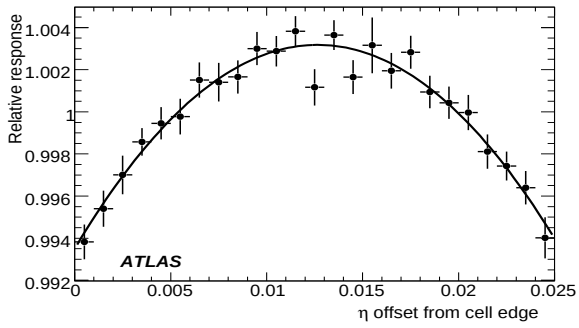

Figure 16: Energy modulation in η for 200 GeV 3×7 electrons, along with the modulation fit [4].

3.2 Cluster energy modulation corrections

As the ϕ impact position of a particle shifts across the accordion structure of the absorbers, the amount of passive absorber material it encounters and thus the ratio $R \equiv E_{\text{reco}}/E_{\text{true}}$ varies slightly, with a periodicity equal to that of the absorber spacing. This effect is small, with a maximum value of about a half-percent. Further, at lower energies, the ϕ position resolution becomes comparable to the absorber spacing; this contributes to washing out the effect at these energies. The reconstructed energy is corrected for this.

To derive the correction, the calorimeter is binned in $|\eta|$. The binning used is not uniform, but is chosen so as to segregate regions of the calorimeter with non-uniform R. Within each $|\eta|$ bin, R is plotted versus the ϕ offset of the cluster relative to the absorber. These plots are divided into ϕ bins, each bin is fit to a Gaussian, and the means of the fits are plotted. The resulting plot is then normalised to unity and fit to a two-term Fourier series:

$$f(\phi) = 1 + A\left[\alpha\cos(N\phi + C) + (1-\alpha)\cos(2N\phi + D)\right], \tag{6}$$

for fit parameters A, α, C, and D. Parameter α is restricted to the range 0–1. N is the total number of absorbers in 2π (1024 in the barrel and 768 in the end-capend-cap). An example of such a fit is shown in Fig. 15.

Fits are performed separately for each energy, cluster size, and particle type. To apply the correction, it is calculated for each η and energy bin. It is then interpolated both in η and in energy. This correction reduces the constant term in the energy resolution (for photons at $|\eta| = 0.3$) from 0.61% to 0.50%.

Energy modulations are also observed along the η direction. The energy of a cluster is defined as the energy within a rectangular window of fixed size in $\eta\times\phi$. The window can only shift by an integral number of cells; however, the impact point of a particle may be anywhere within a cell. Thus, on average, a larger fraction of the cluster energy will be contained in the window when the particle hits at the center of a cell than if it hits near an edge. The size of this effect is a few tenths of a percent, and is larger for smaller cluster sizes. The modulation can be fit well with a quadratic; see Fig. 16. Note that this modulation is very small, $< 0.1\%$, in the ϕ direction, due to increased energy sharing between the cells; this modulation is not presently corrected. (A larger modulation was seen in the test beam [13], which used 3×3 clusters.)

The plots to fit are prepared in a similar manner as for the ϕ modulations, except that the x-axis is taken to be the η offset within a cell. The plots from all bins where the detector is mostly uniform are then combined into a single plot; that is, the $|\eta|$ ranges 0.05–0.75, 0.85–1.30, and 1.70–2.50. The resulting plot is then scaled so as to average to unity and fit to a quadratic. The correction is performed separately for each energy, cluster size, and particle type. The final correction is then determined by

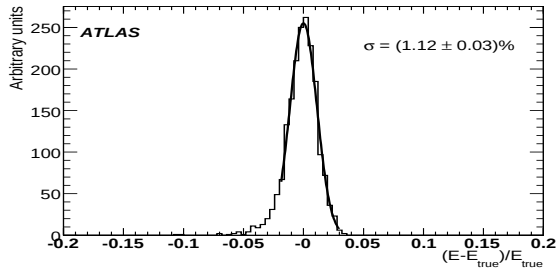

(a) Electrons, $|\eta| = 0.325$.

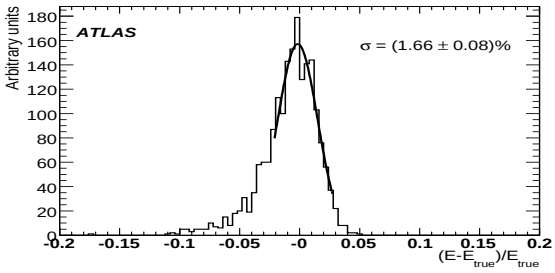

(b) Electrons, $|\eta| = 1.075$.

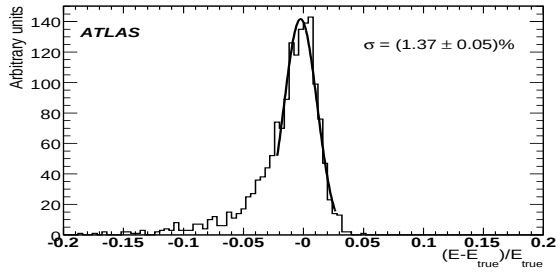

(c) All photons, $|\eta| = 1.075$.

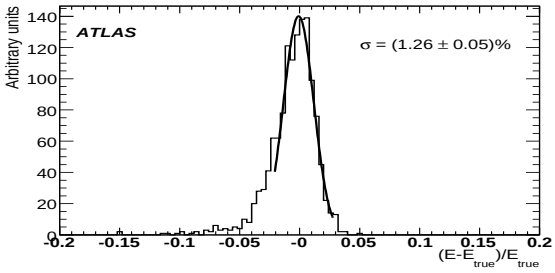

(d) Unconverted photons, $|\eta| = 1.075$.

Figure 17: Difference between measured and true energy normalised to true energy at $E = 100$ GeV.

interpolating in energy. An example fit is shown in Fig. 16. Applying this correction further reduces the constant term to 0.43%. A major contribution to the remaining constant term is from the ϕ-dependency of the inner detector material distribution. (The present weighting correction is averaged over ϕ.)

4 Energy calibration performance

This section shows the performance of the calibration chain used in the current version of the ATLAS reconstruction software used for all of the electron and photon reconstruction and identification studies reported here and elsewhere.

4.1 Single electrons and photons

In Fig. 17, the energy response, plotted as the difference between measured and true energy divided by the true energy, is shown for electrons with an energy of 100 GeV for two illustrative η-positions in the barrel electromagnetic calorimeter. The central value of the energy is reconstructed with excellent precision ($\sim 3 \times 10^{-4}$) if one assumes perfect knowledge of the material in front of the calorimeter. Both the Gaussian core and the non-Gaussian component of the tail of the energy distribution are significantly worse at the point with larger $|\eta|$ due to the larger amount of material in front of the calorimeter. The resolution and non-Gaussian tails are better for photons than for electrons, but are somewhat worse for all photons than for photons that do not convert before leaving the volume of the inner detector.

The linearity (relative difference between the fitted mean energy and the true energy) and resolution are shown in Fig. 18 for electrons and photons. The expected performance is very similar for electrons and photons, with a somewhat larger degradation at larger values of $|\eta|$ in the case of electrons, as expected from the impact of upstream material. For electrons, the linearity is shown for $|\eta| = 0.3$ (barrel) and $|\eta| = 2.0$ (end-cap). The deterioration of the performance seen in the end-cap is attributed to the absence of a presampler ($|\eta| > 1.8$) and the relatively limited statistics of the simulated samples. The

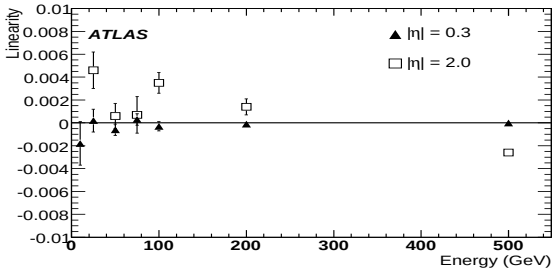

(a) Electron energy linearity.

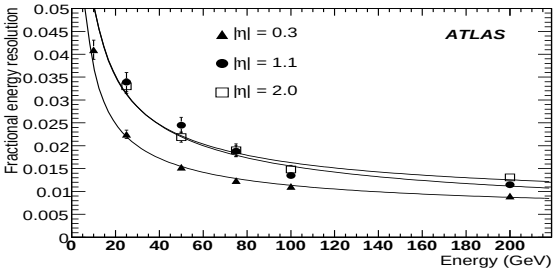

(b) Electron energy resolution.

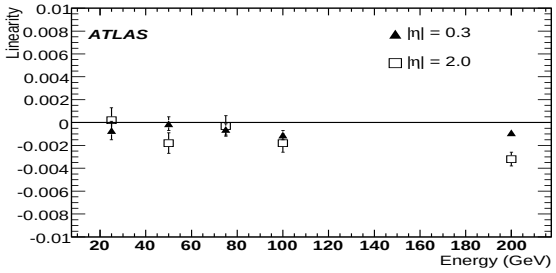

(c) Photon energy linearity.

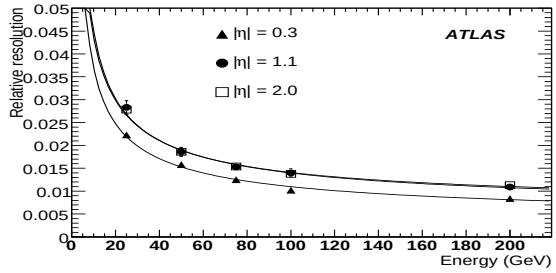

(d) Photon energy resolution.

Figure 18: Energy linearity (left) and resolution (right) for electrons (top) and photons (bottom).

resolution shown in Fig. 18(b) is given for three $|\eta|$ points: $|\eta| = 0.3$ (inner barrel), $|\eta| = 1.1$ (outer barrel), and $|\eta| = 2.0$ (end-cap). The resolution drop at larger $|\eta|$ is attributed to the significant increase of upstream material in front of the calorimeter with respect to the small $|\eta|$ region. The extra material causes increased early showering upstream of the calorimeter, which affects the lateral shower shape in the calorimeter. Since Eq. (4) absorbs the corrections for lateral losses into the overall scale constant A, an increase in lateral-loss fluctuations will result in a deterioration of the resolution. The fits in Fig. 18(b) give a sampling term of $(10.17 \pm 0.33)\%$ at small $|\eta|$, and $(14.5 \pm 1.0)\%$ in the end-cap.

In Fig. 19, the energy resolution for electrons and photons is shown as a function of $|\eta|$. The photon resolution is better than the electron resolution in regions with more material in front of the calorimeter. The extracted constant term of the resolution is shown for photons in Fig. 20 after the weight and modulation corrections. This figure also shows the constant term observed when the standard simulation of cell-level miscalibrations is enabled in the reconstruction program. In Fig. 21, the linearity and resolution as a function of $|\eta|$ is shown for a range of energies for single photons.

4.2 Mass resolution obtained in $H \to 4e$ and $H \to \gamma\gamma$ final states

Figure 22 shows the reconstructed distribution, after calibration, of the invariant mass of the electrons in $H \to 4e$ decays, with $m_H = 130$ GeV. (Loose electron selection applied, as defined in [6].) A global constant term of 0.7% has been included in the electromagnetic calorimeter resolution for the two plots in this subsection. The central value of the reconstructed invariant mass is correct to ~ 1 GeV, corresponding to a precision of 0.7%, and the expected Gaussian resolution is $\sim 1.5\%$. The non-Gaussian tails in the distribution amount to 20% of events lying further than 2σ away from the peak. They are mostly due to bremsstrahlung, particularly in the innermost layers of the inner detector, but also to radiative decays and to electrons poorly measured in the barrel/end-cap transition region of the electromagnetic calorimeter.

Figure 23 shows the reconstructed photon pair invariant mass for $H \to \gamma\gamma$ decays with $m_H = 120$ GeV (tight photon selection applied and barrel/end-cap transition region excluded). The photon directions are

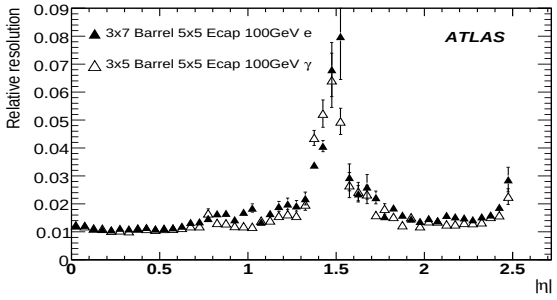

Figure 19: Energy resolution for electrons and photons as a function of $|\eta|$.

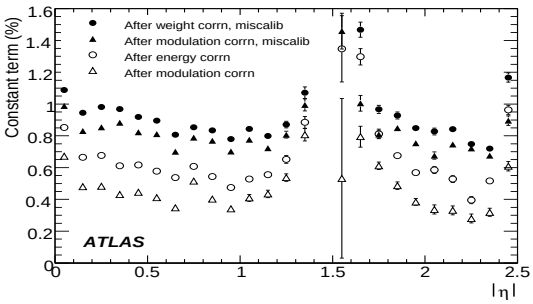

Figure 20: Extracted constant term of the energy resolution for photons, as a function of $|\eta|$, after weight and modulation corrections. Also shown with cell-level miscalibrations enabled.

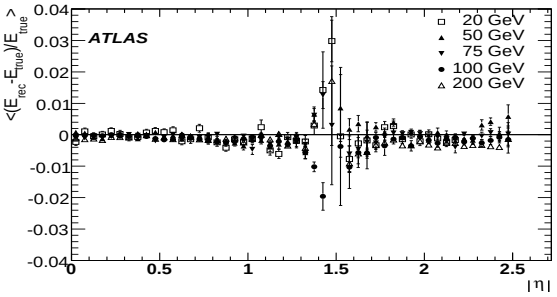

(a) Energy linearity.

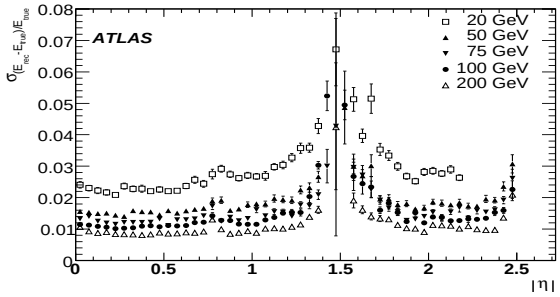

(b) Energy resolution.

Figure 21: Energy linearity and resolution for photons (5×5 clusters).

derived from a combination of the direction measurement in the electromagnetic calorimeter described above (see Section 2.4) with the primary vertex information from the inner detector. The central value of the reconstructed invariant mass is correct to ~ 0.2 GeV, corresponding to a precision of 0.2%, and the expected resolution is $\sim 1.2\%$. Most of the non-Gaussian tails at low values of the reconstructed photon pair mass are seen to be due to photons which convert in the inner detector. The shift in the means comes from the fact that the corrections to-date do not distinguish between converted and unconverted photons.

4.3 Study of systematic effects using $H \to 4e$

The energy linearity for electrons in $H \to 4e$ is shown in Fig. 24(a) for samples based on the ideal (full triangles) and distorted (circles) geometries. The departure from linearity for the distorted geometry is attributed to the presence of extra material in front of the calorimeter. The corresponding resolution is shown in Fig. 24(b) for the distorted geometry.

The uniformity in ϕ and η observed in this sample is shown in Fig. 25. The non-uniformities seen at higher $|\eta|$ and at positive ϕ are due to simulated extra material in these regions. In the ϕ-uniformity plot (Fig. 25(a)) a residual modulation is observed. This is most likely due to an artefact in the simulation. The longitudinal weights used in the reconstruction depend only on η, and are averaged over ϕ. Adding a dependency on ϕ as well would make the energy scale along ϕ more uniform and also improve the mass resolution of $Z \to ee$.

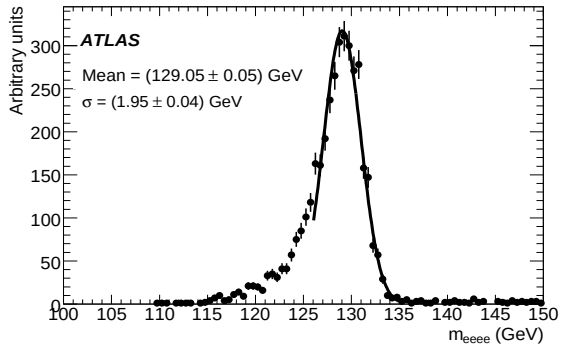

Figure 22: $M(eeee)$ from Higgs boson decays with $m_H = 130$ GeV (energy from calorimeter only, with no Z boson mass constraint).

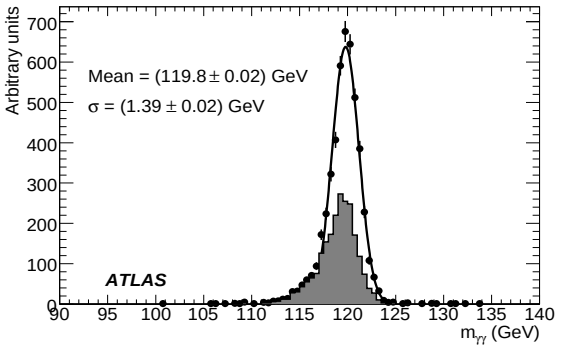

Figure 23: $M(\gamma\gamma)$ from Higgs boson decays with $m_H = 120$ GeV. The shaded plot corresponds to at least one photon converting at $r < 80$ cm.

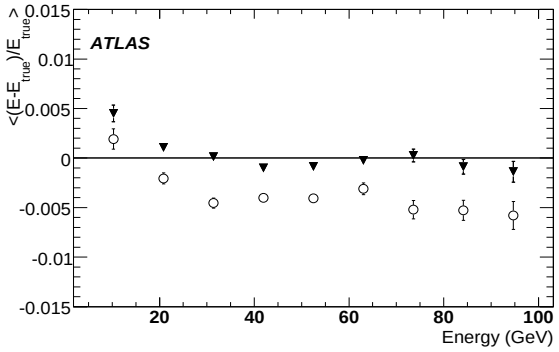

(a) Energy linearity.

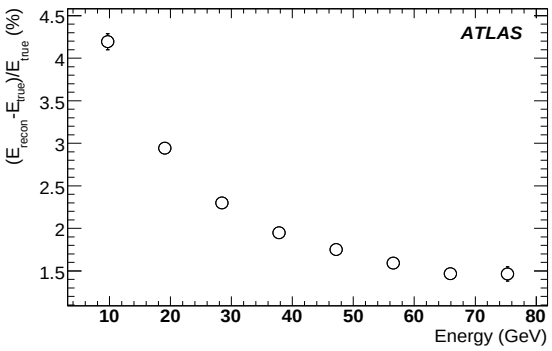

(b) Energy resolution.

Figure 24: Electron linearity and resolution in $H \to 4e$ for the ideal (full triangles) and distorted (circles) geometries.

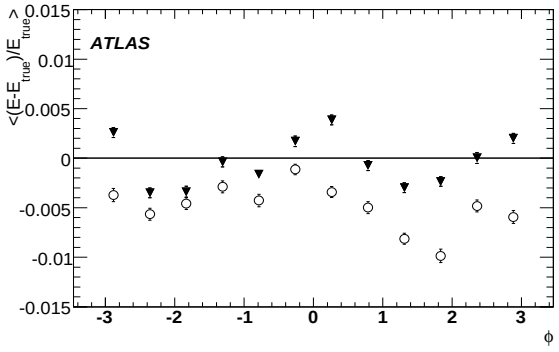

(a) Energy uniformity in ϕ integrated over p_T and η.

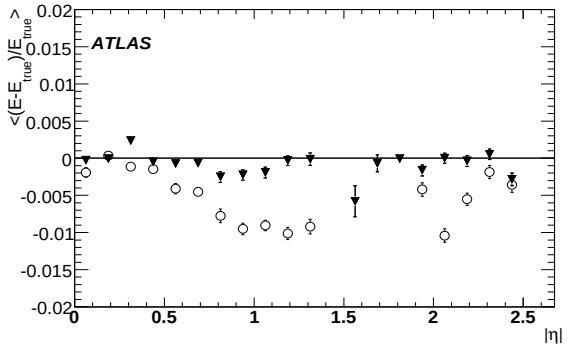

(b) Energy uniformity in η integrated over p_T and ϕ.

Figure 25: Electron energy uniformity in η and ϕ, integrated over other kinematic variables, for the ideal (full triangles) and distorted (circles) geometries.

5 Energy correction using calibration hits

This section describes an alternate method for calculating the total energy from the energies in the individual calorimeter layers and the presampler. It is a development of ideas introduced in [14, 15] to analyse test beam data and is described in some detail in [16]. Special simulations are used in which the energy deposited by a particle is recorded in all detector materials, not just the active ones. Through these simulations, the energy depositions in the inactive material can be correlated with the measured quantities. For example, the energy lost in the material in front of the calorimeter (inner detector, cryostat, etc.) can be estimated from the energy deposited in the presampler. The result is a method which provides a modular way to reconstruct the energies of electrons and photons by decoupling all the different corrections. This approach eases comparisons between electrons and photons, and might be particularly useful in the initial stages of the experiment.

The cluster energy is decomposed into three pieces, which will be treated separately below:

$$E = E_{\text{cal}} + E_{\text{front}} + E_{\text{back}}, \tag{7}$$

where E_{cal} is the energy deposited in the electromagnetic calorimeter, E_{front} is the energy deposited in the presampler and in the inactive material in front of the calorimeter, and E_{back} is the energy that leaks out the rear of the EM calorimeter.

This analysis uses simulated single-particle, mono-energetic electron and photon samples, with energies ranging from 25 to 500 GeV.

5.1 Reconstruction of the energy deposited in the calorimeter

The energy deposited by a particle in the EM calorimeter, E_{cal}, is estimated as

$$E_{\text{cal}} = C_{\text{cal}}(X,\eta)(1 + f_{\text{out}}(X,\eta))E_{\text{cl}}, \tag{8}$$

where

- $E_{\text{cl}} = \sum_{i=1}^{3} E_i$, and $E_{1\ldots3}$ are the energies deposited in each of the three calorimeter layers in a given cluster. In the following, E_{ps} will denote the energy deposited in the presampler. The energies E_i available at this stage of the reconstruction are the energies deposited in the liquid-argon ionisation medium divided by a region-dependent sampling fraction.
- X is the the longitudinal barycentre or shower depth, defined by

  $$X = \frac{\sum_{i=1}^{3} E_i X_i + E_{\text{ps}} X_{\text{ps}}}{\sum_{i=1}^{3} E_i + E_{\text{ps}}}, \tag{9}$$

  where E_i is as above and X_i is the longitudinal depth, expressed in radiation lengths, of compartment i, computed from the centre of the detector. The X_i, which are computed using a geantino[2)] scan, are functions of η.
- η is the cluster barycentre, corrected for the S-shape effect (see Sec. 2.1).
- f_{out} is the fraction of the energy deposited outside the cluster.
- $C_{\text{cal}}(X,\eta)$ is the calibration factor for the energy in the EM calorimeter.

[2)] A "geantino" is an imaginary non-interacting particle used in the simulation. The properties of the material crossed by the particle are recorded.

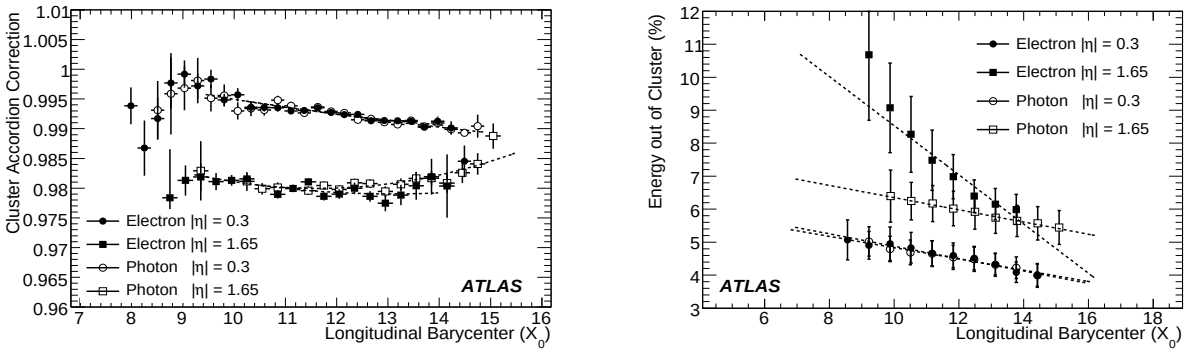

(a) C_{cal} vs. X.

(b) Fraction of out-of-cluster energy.

Figure 26: Correction factor C_{cal} and fraction of out-of-cluster energy as a function of the shower depth X, averaged over all energies, at two representative $|\eta|$ points. The dashed lines show the results of the parametrisation.

The calibration factor C_{cal} is defined as the average ratio between the true energy deposited in the EM calorimeter (both absorbers and ionisation medium) and the reconstructed cluster energy E_{cl}. It is within a few percent of unity, and takes into account effects such as the dependence of the sampling fraction on η and on the longitudinal profile of the shower. Once the correction factor C_{cal} is expressed as a function of X it is fairly energy independent. The correction factor averaged over all energies is shown in Fig. 26(a). Its dependence on X is parametrised with a second order polynomial. The fit is performed excluding the bins with less than 0.5% of the total statistics. This criterion is also applied to all the fits performed in the following.

Due to the presence of the magnetic field and bremsstrahlung radiation, the fraction of energy deposited in the calorimeter outside of the cluster is energy dependent. Since only single electrons and photons with no noise or underlying event are simulated, this fraction is easily calculated. The profile of the out-of-cluster energy is asymmetric with the tail on the high side. However the most probable value, obtained with a Gaussian fit around the maximum of the distribution (-2σ, $+1.5\sigma$), is energy independent when plotted as a function of X. The most probable value of the fraction of energy deposited outside the cluster averaged over all energies is shown in Fig. 26(b) for electrons and photons and the two $|\eta|$ values. Electrons and photons behave similarly in the central region but differently in the forward region. This is due to the large difference in the amount of material present in front of the calorimeter ($\sim 2.5X_0$ at $|\eta| = 0.3$ and $\sim 7X_0$ at $|\eta| = 1.65$) combined with the presence of bremsstrahlung and the magnetic field.

5.2 Energy deposited in front of the calorimeter

The energy lost in the material in front of the calorimeter (inner detector, cryostat, coil, and material between the presampler and strips) is parametrised as a function of the energy lost in the active material of the presampler (E_{ps}):

$$E_{\text{front}} = a(E_{\text{cal}}, \eta) + b(E_{\text{cal}}, \eta)E_{\text{ps}} + c(E_{\text{cal}}, \eta)E_{\text{ps}}^2. \tag{10}$$

An example of this relation is shown in Fig. 27. All coefficients are parametrised in terms of the energy deposited by a particle in the calorimeter (E_{cal}) and η. The coefficient c is used only in the end-cap, $1.55 < |\eta| < 1.8$, and is set to zero otherwise. Note explicitly that E_{front} includes the energy deposited in the presampler and between the presampler and the strips. An alternate form for E_{front},

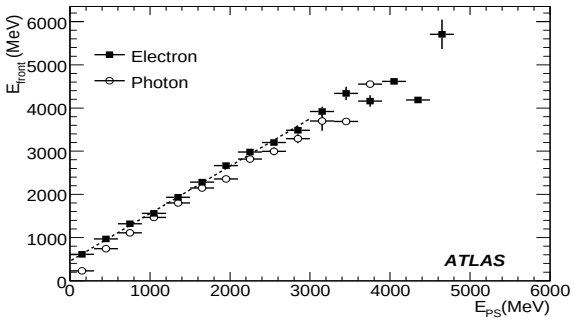

Figure 27: Energy lost in front of the EM calorimeter as a function of the energy measured in the presampler at $|\eta| = 0.3$ for electrons of 100 GeV. The dashed curve shows the parametrisation derived for electrons.

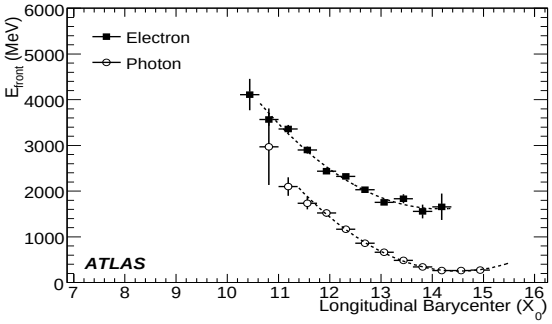

Figure 28: Energy lost in front of the calorimeter as a function of shower depth X, for electrons of 100 GeV at $|\eta| = 1.9$, in a region where the calorimeter is not instrumented with the presampler.

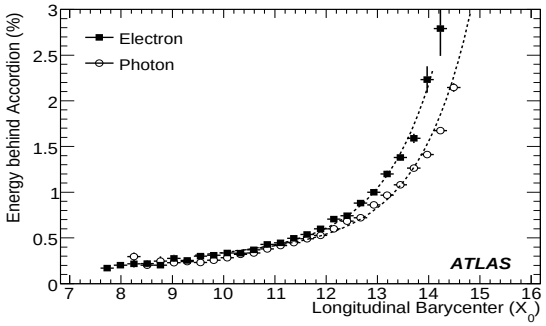

(a) $|\eta| = 0.3$.

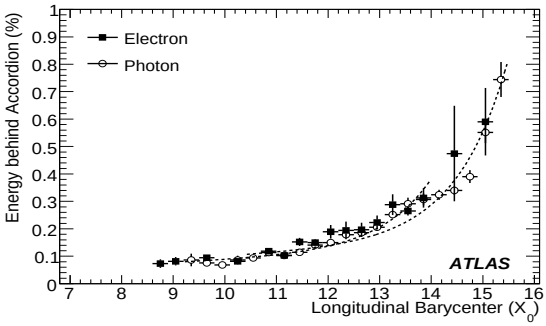

(b) $|\eta| = 1.65$.

Figure 29: Fraction of energy deposited behind the calorimeter, averaged over particle energies, as a function of the shower depth X. The parametrisation used is superimposed.

which depends on the energy in the first calorimeter layer in addition to $E_{\rm ps}$, was also tried. This did not improve the resolution, so the simpler parametrisation above is retained.

In the region $1.8 < |\eta| < 3.2$, not instrumented with the presampler, the energy deposited in front of the calorimeter is parametrised as a function of X with a second degree polynomial. Figure 28 shows this correlation for electrons and photons of 100 GeV at $|\eta| = 1.9$. The coefficients of this polynomial are parametrised in terms of $E_{\rm cal}$.

5.3 Longitudinal leakage correction

The energy deposited by the showers behind the EM calorimeter is computed as a fraction of the energy reconstructed in the calorimeter. This fraction, when parametrised as a function of X, is fairly energy independent both for electrons and photons. Averaged over the particle energies, it is parametrised by

$$f_{\rm leak} \equiv E_{\rm back}/E_{\rm cal} = f_0^{\rm leak}(\eta)X + f_1^{\rm leak}(\eta)e^X. \tag{11}$$

Figure 29 shows the leakage and the result of the fit for $|\eta| = 0.3$ and 1.65.

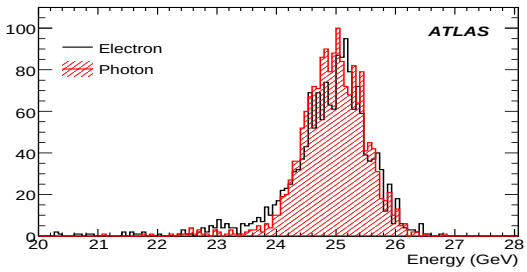

(a) $E = 25$ GeV, $|\eta| = 0.3$.

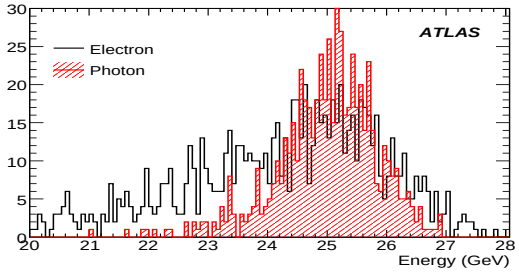

(b) $E = 25$ GeV, $|\eta| = 1.65$.

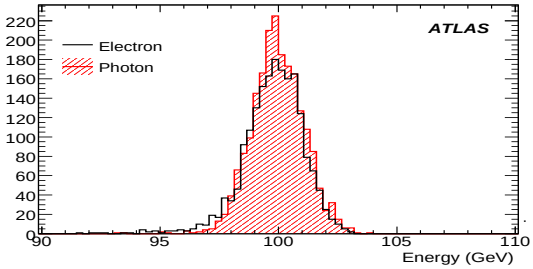

(c) $E = 100$ GeV, $|\eta| = 0.3$.

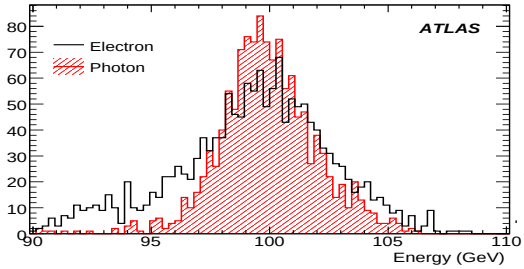

(d) $E = 100$ GeV, $|\eta| = 1.65$.

Figure 30: Total reconstructed energy profiles.

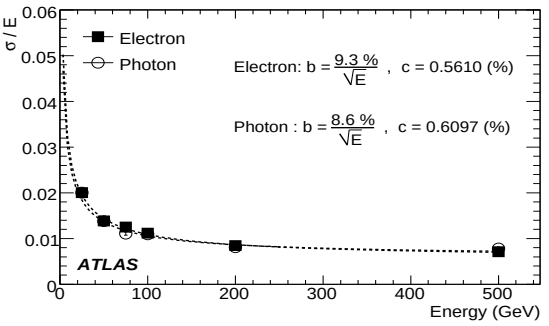

(a) $|\eta| = 0.3$.

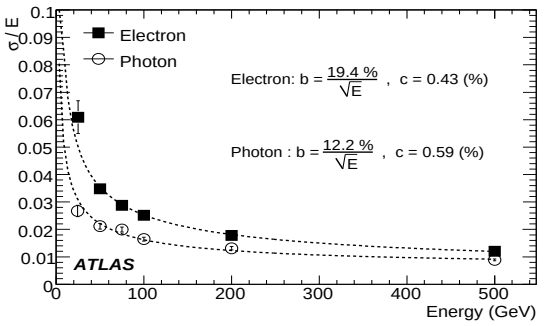

(b) $|\eta| = 1.65$.

Figure 31: Resolution versus particle energy.

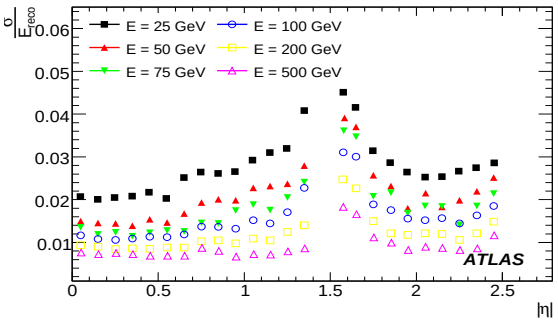

Figure 32: Resolution for various photon energies as a function of $|\eta|$.

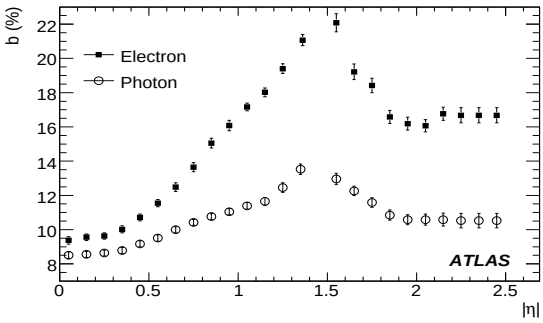

Figure 33: Sampling term as a function of $|\eta|$.

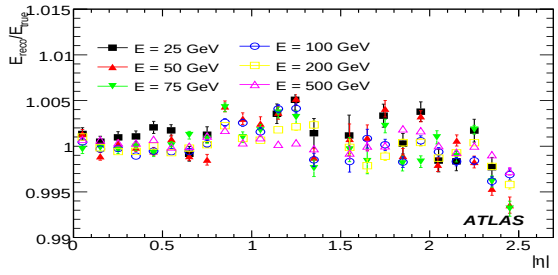

(a) Electrons.

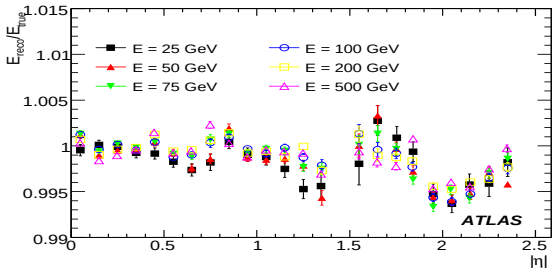

(b) Photons.

Figure 34: Linearity for various particle energies as a function of $|\eta|$.

5.4 Results

The total cluster energy is computed by adding these three contributions. Example distributions of reconstructed energies are shown in Fig. 30. Mean values and standard deviations are found from a fit to a Crystal-Ball function (a Gaussian with a low-side tail of the form $(1-x)^{-n}$).

The resolution is shown in Fig. 31 as a function of the particle energy for electrons and photons at two $|\eta|$ values and in Fig. 32 for various photon energies and all η values. The sampling term is shown in Fig. 33 as a function of $|\eta|$ for electrons and photons.

For electrons, the sampling term increases from 8.7% at low $|\eta|$ to 21% at $|\eta| = 1.55$. This worsening of the energy resolution is related to the increase of the material in front of the calorimeter. This effect is much less relevant for photons, which have a maximum sampling term of 12%. The constant term is in general lower than 0.6% and is related to the energy modulation in a cell (see Sec. 3.2), not corrected at this stage. The linearity, the ratio between the fitted mean value and the true particle energy, is shown in Fig. 34. It is better than 0.5% over the full $|\eta|$ range and in the energy interval 25–500 GeV.

The results from the calibration hits correction are comparable in terms of resolution and linearity with the longitudinal weights method. However there are a few differences worth mentioning. The coefficients of the longitudinal weights method are averaged over a range of energies, while the parametrisations of the calibration hits method are energy dependent. This means that it should be easier to extend the calibrated energy range for the calibration hits method without compromising energy linearity. Another important difference is that while the coefficients of the longitudinal weights method have no direct physical meaning, the parametrisation of the calibration hits method allows isolating the different components of the calibrated cluster energy: that deposited in the calorimeter, inside and outside of the cluster, and in front and behind of it. The knowledge of these separate contributions, which depend on

accurate and detailed simulations of the tracker and the calorimeters, could be particularly useful in the early stages of the experiment, for example to disentangle effects such as a miscalibration of the calorimeter or an imperfect knowledge of the inner detector material. It is also worth noting that the estimate of the energy lost in front of the calorimeter is crucial to obtaining a good resolution and linearity; at low energies and large rapidities, a large fraction of the energy of an electron is deposited in front of the calorimeter. The calculation of missing momentum could also benefit from this separation of effects.

6 In-situ calibration with $Z \rightarrow ee$ events

6.1 Motivation

In the EM calorimeter, the construction tolerances and the calibration system ensure that the response is locally uniform, with a constant term $< 0.5\%$ over regions of size $\Delta\eta \times \Delta\phi = 0.2 \times 0.4$. This has been shown with test beam data [13]. Electron pairs from Z boson decays can then be used to intercalibrate the 384 regions of such size within the acceptance of $|\eta| < 2.4$. These regions must be intercalibrated to within 0.5% in order to achieve a desired global constant term of $< 0.7\%$. The basic idea of this calibration method is to constrain the di-electron invariant mass distribution to the well-known Z boson line shape. A second goal of the calibration is to provide the absolute calorimeter electromagnetic energy scale. This must be known to an accuracy of $\sim 0.1\%$ in order to achieve the ATLAS physics goals[3)].

6.2 Description of the method

Long-range non-uniformities can arise for many reasons, including variations in the liquid argon impurities and temperature, amount of upstream material, mechanical deformations, and high voltage (as localised calorimeter defects may necessitate operating a small number of channels below nominal voltage). For a given region i, we parametrise the long-range non-uniformity modifying the measured electron energy as $E_i^{\text{reco}} = E_i^{\text{true}}(1+\alpha_i)$. Neglecting second-order terms and supposing that the angle between the two electrons is perfectly known, the effect on the di-electron invariant mass is:

$$M_{ij}^{\text{reco}} \simeq M_{ij}^{\text{true}}(1+\frac{\alpha_i+\alpha_j}{2}) = M_{ij}^{\text{true}}(1+\frac{\beta_{ij}}{2}), \tag{12}$$

where $\beta_{ij} \equiv \alpha_i + \alpha_j$.

The method to extract the α's is fully described in [17] and is done in two steps. First, the β's are determined, then the α's. For a given pair of regions (i, j), the coefficient β_{ij} and its associated uncertainty are determined by minimising the following log-likelihood:

$$-\ln L_{\text{tot}} = \sum_{k=1}^{N_{ij}} -\ln L\left(M_k / \left(1+\frac{\beta_{ij}}{2}\right), \sigma_{M,k}\right), \tag{13}$$

where k counts all selected events populating the pair of regions (i, j), M_k is the di-electron invariant mass of event k, and $L(M, \sigma_M)$ quantifies the compatibility of an event with the Z boson line shape and is described below. Fits with only one event are removed. Once the β's are determined from the minimisation, the α's can be found from the overdetermined linear system given by $\beta_{ij} \equiv \alpha_i + \alpha_j$. This is done using a generalised least squares method, and gives an analytic solution.

The Z boson line shape is modeled with a relativistic Breit-Wigner distribution [18, 19]:

$$\text{BW}(M) \sim \frac{M^2}{(M^2 - M_Z^2)^2 + \Gamma_Z^2 M^4 / M_Z^2}, \tag{14}$$

[3)] Except for the W boson mass measurement, which needs a much better knowledge of the energy scale ($\sim 0.02\%$).

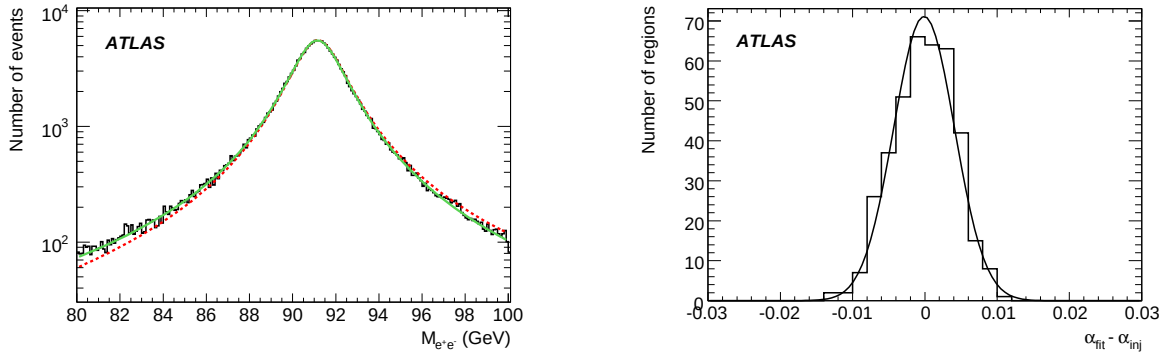

(a) Z line shape

(b) Residual distribution

Figure 35: (a) Z boson mass distribution for PYTHIA events fitted with a Breit-Wigner distribution with (solid line) and without (dashed line) the parton luminosity factor. χ^2/N_{DOF} is 1.09 and 3.96, respectively. (b) Residual distribution fitted with a Gaussian.

where M_Z and Γ_Z are the mass and the width of the Z boson. They were measured precisely at LEP; the values used are, respectively, 91.188 ± 0.002 GeV and 2.495 ± 0.002 GeV [20]. In proton-proton collisions, the mass spectrum of the Z boson differs from the Breit-Wigner shape of the partonic process cross section. The probability that a quark and antiquark in the interacting pp system produce an object of mass M falls with increasing mass. In order to take this into account, the Breit-Wigner is multiplied by the ad-hoc parametrisation $\mathscr{L}(M) = 1/M^{\beta}$. The parton luminosity parameter β is assumed to be a constant and is determined by fitting the Z boson mass distribution obtained with events generated with PYTHIA version 6.403 [21]. Figure 35(a) shows the Z boson mass distribution fitted with a Breit-Wigner with and without the parton luminosity factor. The fitted value of the parameter β is 1.59 ± 0.10; this will be used in the following. Since the photon propagator and the interference term between the photon and the Z boson were not taken into account in the previous parametrisation, the parton luminosity term also accounts for the effects of these two terms.

Finally, in order to take into account the finite resolution of the electromagnetic calorimeter, the Breit-Wigner multiplied by the parton luminosity term is convoluted with a Gaussian:

$$L(M,\sigma_M) = \int_{-\infty}^{+\infty} \mathrm{BW}(M-u)\mathscr{L}(M-u)\,\frac{e^{-u^2/2\sigma_M^2}}{\sqrt{2\pi}\sigma_M}\,du, \tag{15}$$

where σ_M is the resolution of the measured mass. It is related to the electron energy resolution via

$$\frac{\sigma_M}{M} = \frac{1}{2}\sqrt{\left(\frac{\sigma_{E_1}}{E_1}\right)^2 + \left(\frac{\sigma_{E_2}}{E_2}\right)^2}. \tag{16}$$

At $|\eta| = 0.3$, the sampling term of the electron energy resolution is equal to 10.0% and increases with increasing $|\eta|$. Technically, the integral is converted to a discrete summation over the convolution parameter u which takes values between $-5\sigma_M$ and $+5\sigma_M$.

6.3 Generator-level tests

The method is first tested on generator-level $Z \to ee$ Monte Carlo events. These were generated using PYTHIA 6.403 [21] with $M_Z = 91.19$ GeV and $\Gamma_Z = 2.495$ GeV. Events are required to have at least one electron with $p_T > 10$ GeV and $|\eta| < 2.7$ and a di-electron invariant mass $M_{ee} > 60$ GeV. To simulate the detector resolution, generated electron energies are smeared to obtain $\sigma_E/E = 10\%/\sqrt{E/\,\mathrm{GeV}}$.

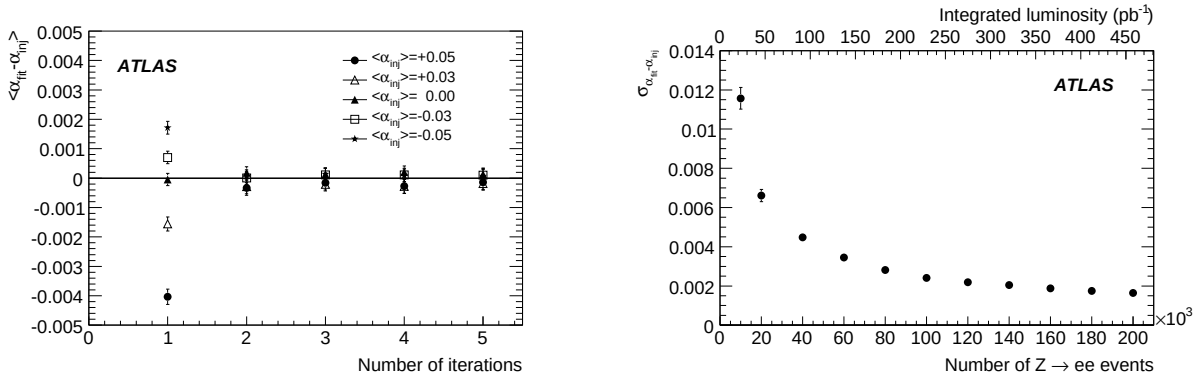

(a) Mean value.

(b) Constant term.

Figure 36: (a) Mean value of the Gaussian fitting the residual distribution as a function of the number of iterations for different mean values of the injected α's; (b) Constant term as a function of the number of events or as a function of the luminosity.

For each calorimeter region i, a bias α_i is generated from a Gaussian distribution with a mean μ_{bias} and width σ_{bias}. These will be called the "injected" α's, α_{inj}.

For the first tests, μ_{bias} is fixed to 0 and σ_{bias} to 2%. The calibration method explained above is applied to 50,000 events after selection. The residual distribution $(\alpha_{\text{fit}} - \alpha_{\text{inj}})$ is shown in Fig. 35(b). The mean value of the residual distribution corresponds to the energy scale, and its width to the energy resolution. Thus it can be seen that the fitting method gives unbiased estimators of the injected α's.

In the case where μ_{bias} is different from zero, the mean value of the residual distribution will be different from zero. For example, for $\mu_{\text{bias}} = -3\%$, $\langle \alpha_{\text{fit}} - \alpha_{\text{inj}} \rangle = 0.1\%$. This is a consequence of neglecting the higher-order terms in the Taylor expansion of Eq. (12). Iterating the procedure twice suffices to recover an unbiased estimate of the α's, as shown in Fig. 36(a).

Figure 35(b) also shows the resulting uniformity. After the fit, the RMS of the distribution has been reduced from 2% to 0.4%. The RMS of the residual distribution is a measure of the expected long-range constant term. Figure 36(b) shows the long-range constant term as a function of the number of reconstructed $Z \to ee$ decays or of the integrated luminosity assuming an event selection efficiency of 25%. Therefore, by summing the local constant term of 0.5% with the long-range constant term of 0.4% obtained here, a total constant term of about 0.7% could be achieved with ~ 100 pb^{-1}. These results assume perfect knowledge of the material in front of the electromagnetic calorimeter.

6.4 Results with distorted geometry

The previous section showed results based on generator-level Monte Carlo. The results in this section use PYTHIA events with full detector simulation and reconstruction, using a geometry with additional material in front of the electromagnetic calorimeter.

The number of events available is 349,450 corresponding to an integrated luminosity of ~ 200 pb^{-1}. Events with at least two reconstructed electrons are kept. The two leading electrons are required to be of at least medium quality [6], to have $p_T > 20$ GeV and $|\eta| < 2.4$, and to be of opposite sign. Finally, the di-electron invariant mass is required to be within $80 < M_{ee} < 100$ GeV. The total selection efficiency is 21.5%; the efficiency for finding two electron candidates within $|\eta| < 2.4$ is 50%.

The calibration method is applied first without injecting any biases ($\alpha_{\text{inj}} = 0$ for all regions). However, the presence of the misalignments and extra material means that there will be some biases intrinsic

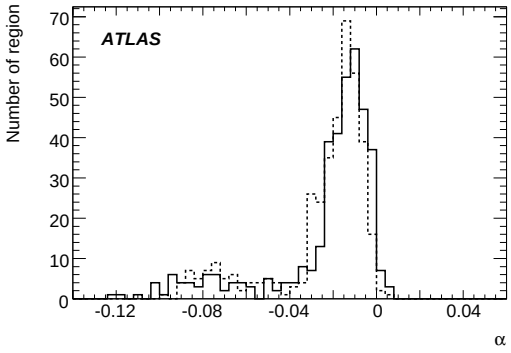

(a) α_{fit} (solid) and α_{true} (dashed).

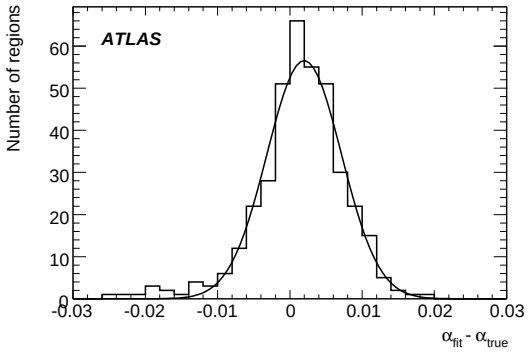

(b) Difference between α_{fit} and α_{true}.

Figure 37: Fit results with distorted geometry and $\alpha_{\text{inj}} = 0$.

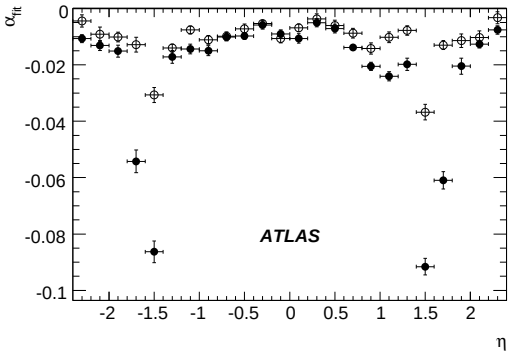

(a) α_{fit} integrated over ϕ as a function of η.

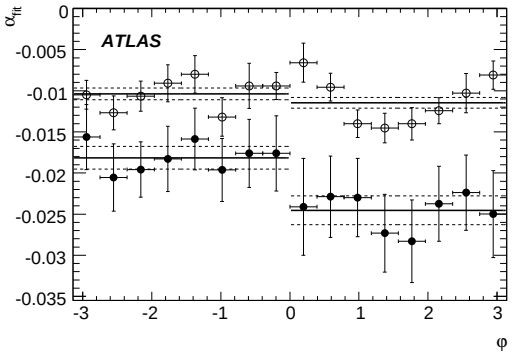

(b) α_{fit} integrated over η as a function of ϕ, fitted in two separate regions.

Figure 38: α_{fit} distributions with $\alpha_{\text{inj}} = 0$ and with distorted/ideal (full/open circles) geometry.

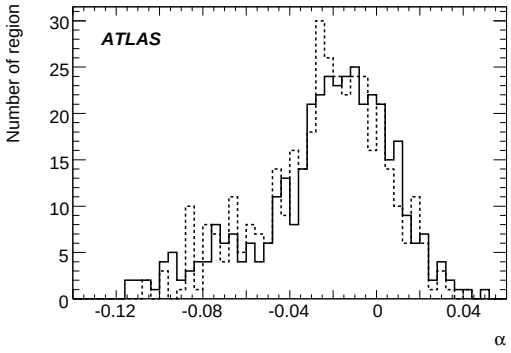

(a) α_{fit} (solid) and $\alpha_{\text{true}} + \alpha_{\text{inj}}$ (dashed).

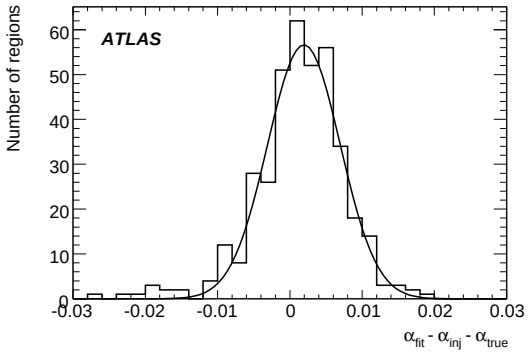

(b) Difference between α_{fit} and $\alpha_{\text{true}} + \alpha_{\text{inj}}$.

Figure 39: Fit results with distorted geometry and additional injected biases.

to the simulation. These "true" biases can be estimated using generator information:

$$\alpha_{\text{true},i} = \frac{1}{N_i} \sum_{k}^{N_i} \frac{p_T^{\text{reco},k} - p_T^{\text{gen},k}}{p_T^{\text{gen},k}}, \tag{17}$$

where k counts over the N_i electrons falling in region i, and $p_T^{\text{reco},k}$ and $p_T^{\text{gen},k}$ are the reconstructed and true transverse momenta of electron k. The distribution of α_{true} is shown in Fig. 37(a), as is the results of the fit. The low-end tail corresponds to regions located in the gap between the barrel and end-cap cryostats (Fig. 38(a)), where the density of material has been increased by a factor of 1.7. There is fair agreement between the α's extracted using the data-driven method and those estimated from generator information. Figure 37(b) shows the difference between α_{fit} and α_{true}; a Gaussian fitted to this distribution has a mean of 0.1% and a width of 0.5%. The distribution of α_{fit} as a function of η and ϕ is shown in Fig. 38 for the ideal and distorted geometries. The asymmetry between positive and negative ϕ is due to the effect of the extra material in the inner detector at positive ϕ. The difference between positive and negative ϕ values is about 0.6%.

The same exercise is also done by introducing, on top of the non-uniformities due to extra material, a bias α_{inj} generated from a Gaussian distribution with a mean $\mu_{\text{bias}} = 0$ and width $\sigma_{\text{bias}} = 2\%$. Results are shown in Fig. 39. The Gaussian fitted to this distribution also has a mean of 0.1% and a width of 0.5%.

One can conclude that, using $\sim 87{,}000$ reconstructed $Z \to ee$ events (which corresponds to about 200 pb^{-1}), and with an initial spread of 2% from region to region, the long-range constant term should not be greater than 0.5%.[4)] This should give an overall constant term $\sim 0.7\%$. The bias on the absolute energy should be small and of the order of 0.2%. If the exercise is repeated with only 100 pb^{-1} of data, the Gaussian fitted to the residual distribution also has a mean of 0.2%, but the width is larger, leading to a long-range constant term of 0.8%.

7 Estimation of the systematic uncertainty on the energy scale

The absolute energy scale has been obtained using electrons from $Z \to ee$ decays. It has been determined on events simulated with the misaligned geometry while the longitudinal weights were found with the ideal geometry. On top of the non-uniformities due to extra material, a bias modeling the calorimeter non-uniformities is introduced and is generated from a Gaussian distribution with a mean $\mu_{\text{bias}} = 0$ and width $\sigma_{\text{bias}} = 2\%$. The resulting bias on the energy scale can be assessed by comparing the fitted α's with those from generator information; the bias is equal to 0.2%. This bias is understood and is due to the fact that the model of the Z boson line shape doesn't take into account the effects of bremsstrahlung. Work is ongoing to improve this issue.

The background has been neglected but it has been checked that the contribution from QCD events where the two jets are misidentified as electrons is small. Thus, it should have a negligible effect on the determination on the energy scale.

Electrons from Z boson decays have a p_T spectrum with a maximum value around 45 GeV. Care will thus have to be taken to extrapolate the calibration obtained from $Z \to ee$ decays to electron energy regions not well populated by these events. Corrections determined with Z boson decays were applied to single electron samples with different generated transverse momenta (20, 40, 120, and 500 GeV) reconstructed with the misaligned geometry. Figure 40 shows $\langle \alpha_{\text{true}} \rangle$ after correction as a function of p_T for four $|\eta|$ bins. In principle, $\langle \alpha_{\text{true}} \rangle$ should be equal to zero. This is true for the 40 GeV electron sample at a level of 0.2% except in the bin ($1.4 < |\eta| < 2.0$) containing the crack region. For central electrons ($|\eta| < 0.6$), the dependence versus p_T is smaller than 0.5%. The effect is worse for non-central electrons.

[4)] Part of the RMS of the residual distribution is also due to uncertainties on the measurement of α_{true}.

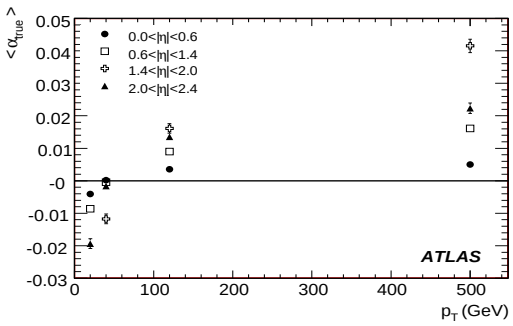

Figure 40: $\langle \alpha_{\text{true}} \rangle$ after correction as a function of p_T for four η bins.

For instance, at $p_T = 120$ GeV, α_{true} after corrections varies from 1 to 1.6 percent. This non-linearity is due to the presence of extra material in front of the calorimeter.

To conclude, at the Z boson energy scale, the estimate of the systematic uncertainty is around 0.2%. At other energy scales, the systematic uncertainty is dominated by effects of extra material. For central electrons, corrections can be extrapolated over the full p_T spectrum to a level of 0.5%. The linearity is degraded for non-central electrons at a level of 1 or 2 percent except in the crack region where it is worse. These numbers depend on the amount of extra material added to the misaligned geometry compared to the ideal geometry and will likely be different with real data.

The performance presented here corresponds to our current understanding of the determination of the absolute energy scale. Improvements are expected to achieve systematic uncertainties smaller than 0.5%. For instance, including information from the E/p ratio measured for isolated high-p_T electrons from $W \to e\nu$ decays will compliment the direct calibration of the absolute scale with $Z \to ee$ events. Photon conversions can also help to determine the amount of material in front of the calorimeter.

Conclusion

The methods and algorithms described in this note were already mentioned in Ref. [1] many years ago. Over the years, they have reached a higher level of stability and maturity, and have been implemented in the ATLAS reconstruction software. It is believed that, given the constraints of the ATLAS detector, in particular the amount of dead material in front of the calorimeter, the performances described here will not evolve much further.

The real challenge at the beginning of data-taking will be the detection and correction for additional inner detector material or calorimeter inhomogeneities which would not have affected the somewhat smaller-scale detectors used in the test beam. Discrepancies between data and simulation will have to be understood prior to the use of the methods described above. The in-situ calibration with $Z \to ee$ events described in Section 6 will play an important role, and refinements of the method presented here are expected.

References

[1] ATLAS Collaboration, Detector and Physics Technical Design Report, Vol.1, CERN/LHCC/99-14 (1999).

[2] ATLAS Electromagnetic Liquid Argon Calorimeter Group (B. Aubert et al.), Nucl. Inst. Meth. **A500** (2003) 202–231.

[3] ATLAS Electromagnetic Liquid Argon Calorimeter Group (B. Aubert et al.), Nucl. Inst. Meth. **A500** (2003) 178–201.

[4] ATLAS Collaboration, G. Aad et al., The ATLAS experiment at the CERN Large Hadron Collider, 2008 JINST 3 S08003 (2008).

[5] W. Lampl et al., Calorimeter Clustering Algorithms: Description and Performance, ATLAS-LARG-PUB-2008-002 (2008).

[6] ATLAS Collaboration, Reconstruction and Identification of Electrons, this volume.

[7] ATLAS Collaboration, Reconstruction and Identification of Photons, this volume.

[8] ATLAS Collaboration, Liquid Argon Calorimeter Technical Design Report, CERN/LHCC/96-41 (1996).

[9] GEANT Detector Description and Simulation Tool, 1994, CERN Program Library Long Write-up W5013.

[10] M. Aleksa et al., Report ATL-LARG-PUB-2006-003, 2006.

[11] R. Sacco et al., Nucl. Inst. Meth. **A500** (2003) 178–201.

[12] S. Paganis, Nucl. Phys. Proc. Suppl. **172** (2007) 108–110.

[13] M. Aharrouche et al., Nucl. Inst. Meth. **A582** (2007) 429–455.

[14] M. Aharrouche et al., Nucl. Inst. Meth. **A568** (2006) 601–623.

[15] G. Graziani, Report ATL-LARG-2004-001, 2004.

[16] L. C. D. Banfi and L. Mandelli, Report ATL-LARG-PUB-2007-012, 2007.

[17] F. Djama, Report ATL-LARG-2004-008, 2004.

[18] F. Berends et al., in *Z* physics at LEP 1, ed. G. Altarelli, R. Kleiss, and C. Verzegnassi, (CERN Report 89-08, 1989).

[19] LEP Electroweak Working Group, Phys. Rep. **427** (2006) 257.

[20] Particle Data Group (S. Eidelman et al.), Phys. Lett. **B592** (2004) 1.

[21] T. Sjöstrand et al., Comp. Phys. Comm. **135** (2001).